Journal of The Electrochemical Society

The Electrochemical Society
Advancing solid state & electrochemical science & technology

OPEN ACCESS

Large-Format Bipolar and Parallel Solid-State Lithium-Metal Cell Stacks: A Thermally Coupled Model-Based Comparative Study

To cite this article: Mei-Chin Pang *et al* 2020 *J. Electrochem. Soc.* **167** 160555

View the article online for updates and enhancements.

240th ECS Meeting
Oct 10-14, 2021, Orlando, Florida
Register early and save up to 20% on registration costs
Early registration deadline Sep 13
REGISTER NOW



This content was downloaded from IP address 155.198.10.231 on 02/08/2021 at 15:12

Journal of The Electrochemical Society, 2021 **167** 160555

Large-Format Bipolar and Parallel Solid-State Lithium-Metal Cell Stacks: A Thermally Coupled Model-Based Comparative Study

Mei-Chin Pang,[1] Youxiu Wei,[2,3] Huizhi Wang,[1] Monica Marinescu,[1] Yue Yan,[2,3] and Gregory J. Offer[1,z]

[1]*Department of Mechanical Engineering, Imperial College London, Exhibition Road, South Kensington Campus, London, SW7 2AZ, United Kingdom*
[2]*Beijing Institute of Aeronautical Materials (BIAM), P.O. Box 81-83, Beijing 100095, People's Republic of China*
[3]*Beijing Engineering Research Centre of Advanced Structural Transparencies for the Modern Traffic System, P.O. Box 81-83, Beijing 100095, People's Republic of China*

Despite the potential of solid electrolytes in replacing liquid electrolytes, solid-state lithium-metal batteries have not been commercialised for large-scale applications due to manufacturing constraints. In this study, we demonstrate that the desired energy and power output for large-format solid-state lithium-metal batteries can be achieved by scaling and stacking unit cells. Two stack configurations, a bipolar and a parallel stack are modelled and compared. With 63 cells stacked in series, we show that a bipolar stack could reach a stack voltage up to 265 V. In contrast, a parallel stack with 32 double-coated cells could achieve a nominal capacity of 4 Ah. We also demonstrate that the choice of current collectors is critical in determining the gravimetric power and energy density of both stacks. By coupling the electrochemical stack model thermally, we show that the Joule heating effects are negligible for bipolar stacks but become dominant for parallel stacks. Bipolar stacks are better due to their higher power and energy densities and lower heat generation, but a lower Coulombic stack capacity limits their performance. In contrast, parallel stacks generate more heat and require more advanced thermal management. These thermally-coupled stack models can be used as prototypes to aid the future development of large-format solid-state batteries.
© 2021 The Author(s). Published on behalf of The Electrochemical Society by IOP Publishing Limited. This is an open access article distributed under the terms of the Creative Commons Attribution 4.0 License (CC BY, http://creativecommons.org/licenses/by/4.0/), which permits unrestricted reuse of the work in any medium, provided the original work is properly cited. [DOI: 10.1149/1945-7111/abd493]

Manuscript submitted August 20, 2020; revised manuscript received November 23, 2020. Published January 14, 2021.

The research on inorganic Solid Electrolyte (SE) such as sulfide- and oxide-based electrolytes has been gaining significant momentum due to the non-flammable features of the electrolytes.[1–5] Compared to the combustible aprotic organic electrolytes, solid-state Li-metal batteries provide potential solutions to the critical safety issues faced by conventional Li-ion batteries such as thermal runaway.[6] However, solid-state Li-metal batteries have not been implemented for large-scale applications such as powertrain electrification due to scaling and manufacturing limitations.[7,8] Capacity of a single-layer cell is insufficient to meet the power demands. Overcoming the up-scaling and manufacturing barriers is, therefore, an absolute prerequisite to enable the large-scale applications of solid-state Li-metal batteries.

One possible method to increase the total power and energy output of solid-state Li-metal batteries is to scale and stack each unit cell in series or in parallel. In series stacking each unit cell is connected by the Bipolar Plates (BP), whereas in a parallel stacking the Current Collectors (CC) and tabs of each unit cell are connected together to form a stack. Toyota built the prototype of bipolar solid-state cell stack and showed that it is possible to obtain a maximum voltage of 16.26 V by stacking four layers of single unit cells.[9] Gambe et al.[10] have also developed a bipolar stack based on quasi-solid-state electrolyte and demonstrated a stack voltage experimentally up to 12 V. Ito et al.[11] have constructed a parallel solid-state cell stack by stacking three double-coated unit cells to achieve a capacity of 1 Ah.

While bipolar and parallel stack configurations have been proposed and measured experimentally, no systematic comparison between these two configurations is available in terms of their advantages and limitations. By identifying the scaling factor from a system of dimensionless governing equations, we propose a model-based approach to study the effects on performance from upscaling parallel and bipolar stacks. Based on the Ragone analysis, we compare the volumetric as well as the gravimetric energy and power densities of both stack profiles. The impact of CC in a single-layer cell is negligible due to their high electronic conductivity and negligible mass. However, as the number of unit cells in the stack increases, the mass and volume ratio of the CC can play a significant role in determining the stack's energy and power density. We demonstrate in this study that the choice of CC is critical in optimising the stack performance.

While the heat generation in a single-layer cell is insignificant due to the large surface-to-volume ratio, the impacts of heat generation in a stack can be significant and affect the stack performance. Toyota has confirmed that their prototyped all-solid-state stack can be operated at a temperature of 100 °C.[9] The effects of such high operating temperature on the internal heat generation and electrochemical stack performance of the bipolar and parallel configurations have not been studied. Recently, Bock et al.[12] proposed an analytical stack model comprising of 24 cells to study the temperature distribution at the stack centre and outer boundary. However, the analytical thermal model was not coupled with the electrochemical model. As a result, the values for the heat sources used in the thermal model were not calculated from the electrochemical model, and the stack performance also did not account for the impacts of heat generations. We address this gap by proposing a coupled electrochemical stack model with a two-dimensional thermal model, enabling the comparison of the heat generation and temperature gradients for stacks of different configurations.

Model Development

Temperature-dependent single-layer cell model.—The one-dimensional single-layer model developed by Offer et al.[13] was improved to provide a framework to study the effects of different operating temperatures on the heat generations. Figure 1 illustrates the model domain of a single-layer cell. The temperature dependence is included in the following parameters: the Open-Circuit Potential (OCP) of the cell, ionic conductivity in the SE, exchange current densities at the electrode-electrolyte interfaces and solid diffusion in the Positive Electrode (PE). Secondly, due to the relatively small surface over-potential at the Negative Electrode (NE) and SE interface,[13] the Butler-Volmer expression describing the kinetics at this interface is linearised to[14,15]

$$i = i_{0,\mathrm{neg}}(\overline{T})\frac{(\alpha_\mathrm{a} + \alpha_\mathrm{c})F}{R_\mathrm{gas}\overline{T}}\eta_\mathrm{neg} \qquad [1]$$

where $i_{0,\mathrm{neg}}(\overline{T})$ is the temperature-dependent exchange current density at the NE interface, α_a and α_c are the charge-transfer coefficient

[z]E-mail: gregory.offer@imperial.ac.uk

($\alpha_a = \alpha_c = 0.5$), F is the Faraday's constant ($F = 96,485\ \mathrm{C\ mol^{-1}}$), R_{gas} is the universal gas constant ($R_{gas} = 8.314\ \mathrm{J\ K^{-1}\ mol^{-1}}$), $\overline{T}$[K] is the average temperature evaluated from the two-dimensional thermal model and η_{neg} is the overpotential at the NE interface.

The overpotential at the PE side is higher than that at the NE interface.[13] Therefore, the kinetics can be considered as irreversible, represented here by the Tafel equation[14,15]

$$i = -i_{0,pos}(\overline{T})\left(\frac{c_{Li,surf}}{c_{bulk}}\right)\exp\left(\frac{-\alpha_c F\eta_{pos}}{R_{gas}\overline{T}}\right), \quad [2]$$

where $i_{0,pos}$ is the concentration and temperature-dependent exchange current density, given by:

$$i_{0,pos} = Fk_{pos}(\overline{T})\left(\frac{c_{LCO,max} - c_{bulk}}{c_{LCO,max}}\right)^{0.5}\left(\frac{c_{bulk}}{c_{LCO,max}}\right)^{0.5} \quad [3]$$

The exchange current density can be defined as the current density at equilibrium, under which the rate of the forward reaction is equal to the rate of the backward reaction.[14] Therefore, c_{bulk} represents the average bulk Li concentration and can be calculated by averaging the concentration distribution within the PE domain ($c_{bulk} = \overline{c}_{Li}$). However, as the current density described by the Tafel's equation is irreversible, the inclusion of concentration-dependence to the PE kinetics should be further assessed by comparison to additional experiments in the future. $c_{LCO,max}$ is the theoretical molar density of the $LiCoO_2$PE ($c_{LCO,max} = 51599.06\ \mathrm{mol\ m^{-3}}$).[13] k_{pos} is the temperature-dependent rate-constant (see Appendix A), and η_{pos} is the overpotential at the PE-SE interface. The term ($c_{Li,surf}/c_{bulk}$) in Eq. 2 accounts for the contribution of the concentration gradient due to the diffusion in the PE to the rate of Li flux between the SE and the PE. Figure A·1a in Appendix A compares this ratio for three current densities (0.1C, 1C and 5C). For low current densities (⩽1C), this term can be approximated as unity. The flux of Li between the SE and the PE is driven predominantly by the charge-transfer reaction. However, as the current densities increase, the rate of Li flux is controlled by both charge-transfer and diffusion mechanisms, and the contribution of the solid concentration gradient cannot be neglected.

A summary of the modified governing equations can be found in Appendix A. The model predictions for the single-layer cell with temperature-dependent parameters were first compared with the experimentally measured discharge curves at four operating temperatures. The model was then scaled for a stack by adjusting the electrode active area. This scaling approach was derived based on the experimental work of Ito et al.,[11] in which they scaled a pelletised cell to a practical size. The surface area is chosen based on a commercial Li-ion polymer battery (EiG C020).[16] Through the dimensionless governing equations, we show in Appendix A that scaling the electrode active surface area only affects the current density. The system of governing equations was non-dimensionalised (detailed in Appendix A) to identify the scaling factor and assess the influence of scaling the electrode active area on the model parameters. If the materials, electrode composition and the manufacturing process are the same for the small-scale and large-scale cells, Kim et al. demonstrated that the model parameters used for small-scale cells could be used for large-scale cells.[17] Therefore, the nominal current of the single-layer scaled cell, $I_{cell,scaled}$, can be determined from

$$I_{cell,scaled} = i_{cell,ref} \times A_{ref}, \quad [4]$$

in which $i_{cell,ref}$ is the reference current density of the experimental cell and A_{ref} is the surface area of our reference cell.

Working principles of bipolar and parallel stacks.—A stack comprises multiple single-layer cells. Generally, there are two types of stacks: bipolar and parallel,[10,18–20] as shown in Fig. 2.

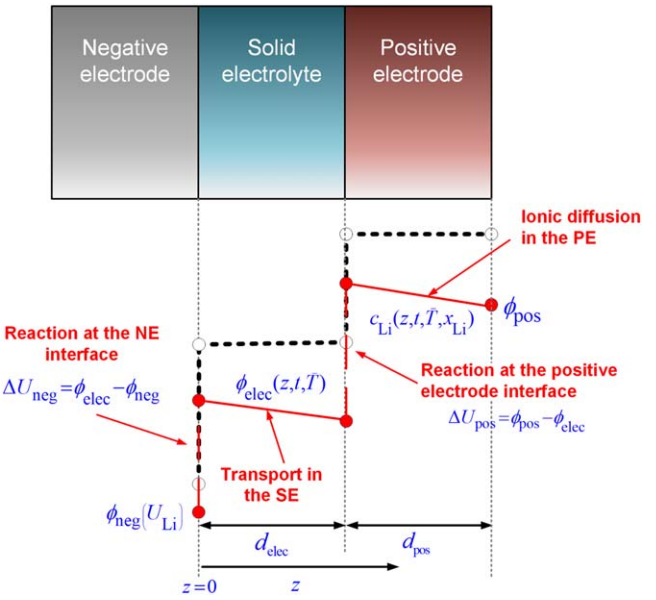


Figure 1. Illustration of the temperature-dependent single-layer model domain in the z-direction, where z denotes the spatial variation, t represents time, $\overline{T}$ indicates the temperature dependence and c_{Li} represents the concentration of Li^+ in the PE. The dashed lines and empty circles indicate the open-circuit states, whereas the red solid lines and filled circles denote the computational states under load. The potential differences due to interfacial charge-transfer kinetics are given by ΔU_{neg} and ΔU_{pos}. ϕ_{elec} denotes the electrolyte potential, whereas ϕ_{neg} and ϕ_{pos} represent the NE and PE electrode potentials, respectively. U_{Li} is the equilibrium potential of Li-metal.

In a bipolar stack, each unit cell is connected in series through the BP, with the PE material coated to one side of the plate and the NE material coated to the opposite side of the plate. An electrical insulator such as the fluoroelastomer seal is used to separate the adjacent BP from a direct contact and to prevent an internal short-circuit.[18,21] In addition, the BP must be free from pinholes to prevent a short between the electrode materials on both sides.[18,22] However, the BP must have high electronic conductivity to allow the flow of electrical current between adjacent cells and be electrochemically inert at the same time to prevent any side reactions with the electrode materials on both sides. In terms of mechanical properties, the BP must be ultrathin and lightweight to minimize the stack overall volume and weight. The BP must also have a high mechanical strength to maintain the integrity of the cell under extreme operating conditions such as overcharge, overdischarge or high operating temperatures.[18] Examples of BP materials include aluminum foils,[19,21] modified titanium foils,[23] carbon composites,[18] copper/aluminum bimetallic substrates[24] and SUS stainless steels.[10,25,26]

In a parallel stack, each unit cell consists of PE and NE materials separated by the SEs with CC at both ends of the single unit cell. For a double-coated cell configuration, the PE material is coated to both sides of the positive CC.

There are two streams of current flow in a cell operation, given by the migration of Li-ions (the ionic current) and by the transport of electrical charges (i.e. the electrical current).[20] In the bipolar stack, the electrical current of unit cells flows perpendicular through the BP. In the parallel stack, the ionic current flows perpendicular from the NE to the PE. In contrast, the electrical current of all cells flows perpendicular and in-plane along the CC to the external tabs.

Stack model.— *One-dimensional bipolar stack model.*—In a one-dimensional bipolar stack model, each single-layer scaled cell is stacked in series to achieve a bipolar configuration, as shown by Fig. 3a. The governing equation to describe the relationship between the stacked and unit cell voltage is the Kirchhoff's voltage law.

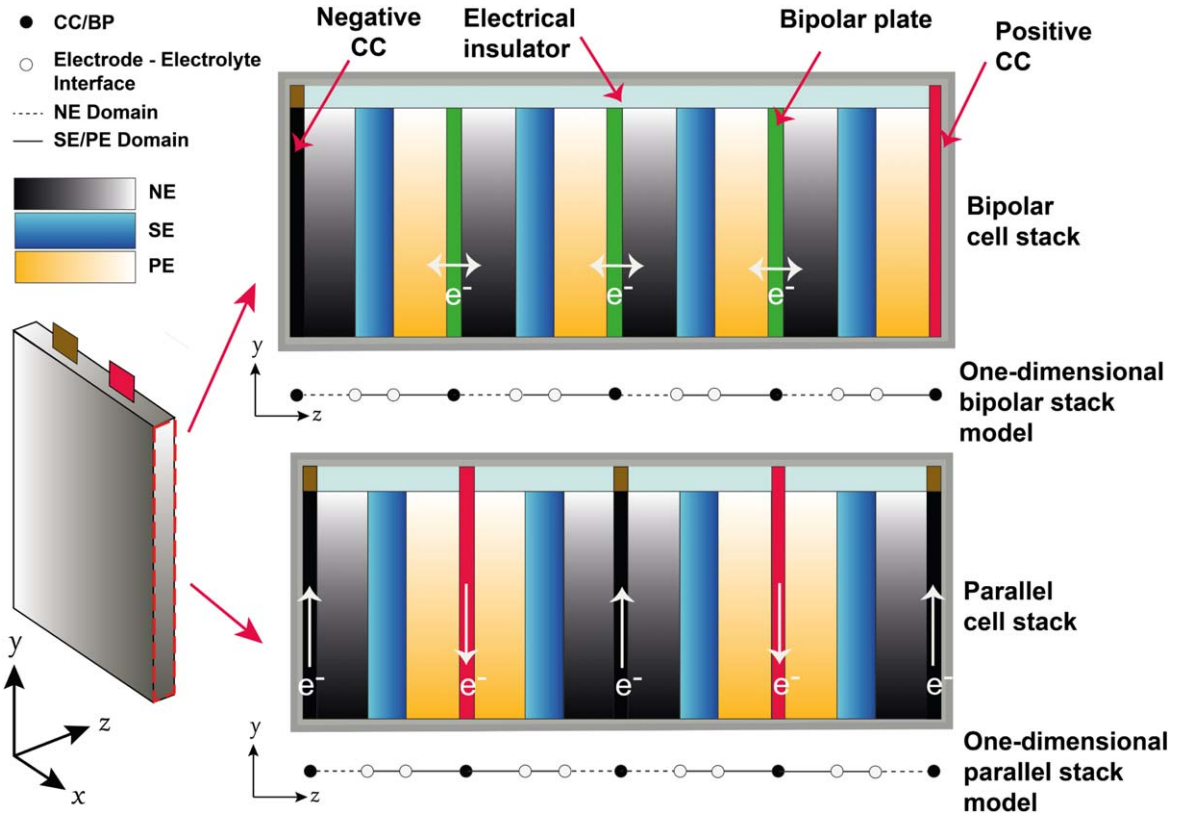


Figure 2. Configurations of the bipolar (top) and parallel stack (bottom) inside the pouch. In a bipolar stack, the electrical current flows from one unit cell to the adjacent unit cell through the BP, whereas in a parallel stack, the electrical current flows in-plane along the CC to the external tabs. The one-dimensional bipolar stack model is constructed by stacking the SE and PE domains (solid lines). The NE domain (dashed line) is represented by an interfacial point between the NE and the SE. The one-dimensional parallel stack model consists of the double-coated cells arranged in parallel. The filled circle symbols represent the BP in the bipolar stack model and CC in the parallel stack model, whereas the empty circles denote the electrode-electrolyte interfaces.

Assuming a negligible cell-to-cell variation in a perfect stack, the total stacked voltage can be calculated by multiplying the number of cells with the individual cell voltage. Therefore, the open-circuit voltage of the bipolar stack, $U_{\text{stack,BP,OCV}}$ can be calculated by

$$U_{\text{stack,BP,OCV}} = N_{\text{BP}}(\phi_{\text{pos}} - \phi_{\text{neg}}), \quad [5]$$

where N_{BP} is the number of unit cells in a bipolar stack. Because the single-layer cells are connected in series and form part of the same circuit loop, the same current must flow through each unit cell, as given by

$$i_{\text{stack,BP}} = i_{\text{cell}}, \quad [6]$$

where i_{cell} is the current density of each unit cell.

The electrochemical behavior of the stack was considered as a one-dimensional model in the z-direction (refer to Fig. 2 for the definition of the coordinates). As shown by Yazdanpour et al.,[20] the in-plane current density $i = (i_x, i_y, 0)$ corresponds to the transport of electrons in the active materials and CC, whereas the through-plane current density, $i = (0, 0, i_z)$ denotes the transport of Li-ions. In this work, the ohmic losses due to electronic transport are lumped together and subtracted from the final stack voltage. The stack voltage, V_{BP} under load can be calculated by

$$V_{\text{BP}} = N_{\text{BP}}(\phi_{\text{pos}} - \phi_{\text{neg}}) - i_{\text{stack,BP}}R_{\text{stack,BP}}, \quad [7]$$

where $R_{\text{stack,BP}}$ is the sum of all ohmic resistances in a bipolar stack:

$$R_{\text{stack,BP}} = N_{\text{BP}}R_{\text{BP}} + N_{\text{BP}}R_{\text{AM}} + R_{\text{tab,pos}} + R_{\text{tab,neg}}. \quad [8]$$

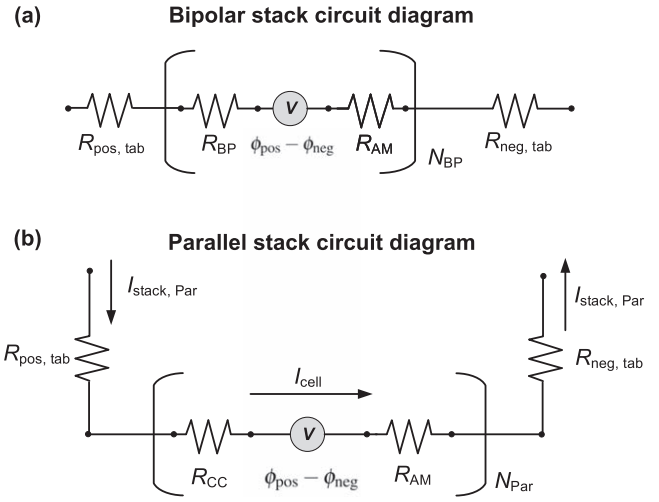


Figure 3. (a) Representative bipolar stack circuit diagram, where the ohmic resistances of the bipolar stack include a positive tab resistance ($R_{\text{pos,tab}}$), a negative tab resistance ($R_{\text{neg,tab}}$), ohmic resistances due to BP, R_{BP} and ohmic resistances due to electronic transport across the electrodes (R_{AM}). (b) The parallel stack circuit diagram includes ohmic resistances from positive and negative tab resistances ($R_{\text{pos,tab}}$ and $R_{\text{neg,tab}}$), ohmic resistances due to the electronic transport in the CC, R_{CC} and electrodes, R_{AM}.

As shown by Figs. 2 and 4a, the current flows normal to the stack surface area in a bipolar stack and is distributed uniformly over them. Therefore, the ohmic resistance across the BP, R_{BP} can be calculated as follows:

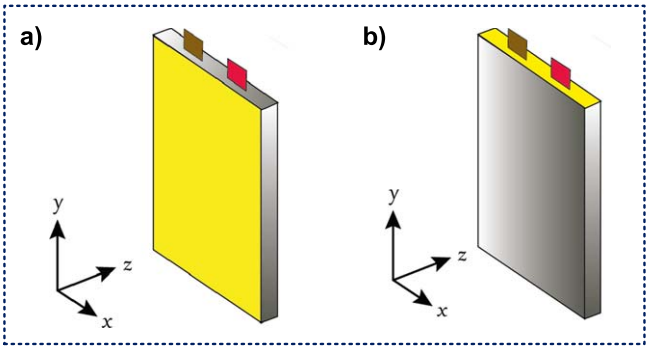


Figure 4. (a) The electrical current flows perpendicular to the stack surface area in a bipolar stack. (b) In a parallel stack, the electrical current flows perpendicular to the CC and then in-plane along the CC to the external tabs or vice versa. In both stack configurations, the cross-sectional area, A_i is defined by the surface normal to the current flow (yellow coloured area), whereas the length, L_i is defined by the dimension along the current flow.

$$R_{BP} = \frac{d_{BP}}{\sigma_{BP} A_{BP}}, \quad [9]$$

in which d_{BP} is the thickness of the BP, σ_{BP} is the electronic conductivity of the BP and A_{BP} is the stack surface area. Because the current is flowing only in one direction through the BP in the middle of the stack, the calculation of the bipolar stack resistance can be simplified into a one-dimensional resistance, given by Eq. 9. However, at the first and last unit cell of the bipolar stack, the current is flowing perpendicular and in-plane to the external tabs or vice versa. Due to the negligible impacts of the total resistance from the first and last CC, we simplify the current flow behavior in these two CC into a one-dimensional electronic transport like all the other BP.

In Ref. 13 the ohmic resistance across both non-porous PE and NE was not considered in the single-layer model due to the relatively small size of the cell and a limited magnitude of applicable current densities. As a result, the voltage loss due to electronic transport in both electrodes was found to be negligible. However, as the cell is scaled and stacked to model a large-format solid-state bipolar and parallel stack, the impacts of electronic transport resistance across both electrodes cannot be neglected. Hence, the ohmic resistance across the PE and NE, R_{AM} can be considered in the large-format stack models through

$$R_{AM} = \frac{d_{neg}}{\sigma_{neg} A_{neg}} + \frac{d_{pos}}{\sigma_{pos} A_{pos}}, \quad [10]$$

in which d_{neg} is the thickness of the NE, σ_{neg} is the electronic conductivity of metallic Li, d_{pos} is the thickness of the PE and σ_{pos} is the electronic conductivity of $LiCoO_2$. The subscript AM represents the active materials in both electrodes.

Based on the direction of current flow into and out of the tabs, the ohmic resistance of the positive tab ($R_{tab,pos}$) and negative tab ($R_{tab,neg}$) can be calculated as follows:

$$R_{tab,pos} = \frac{L_{tab,y}}{\sigma_{tab,pos} A_{tab,cross}}, \quad [11]$$

$$R_{tab,neg} = \frac{L_{tab,y}}{\sigma_{tab,neg} A_{tab,cross}}, \quad [12]$$

where $L_{tab,y}$ is the height of the tabs; $\sigma_{tab,pos}$ and $\sigma_{tab,pos}$ are the electronic conductivities of the positive and negative tabs; $A_{tab,cross}$ is the cross-sectional area of the tab. It should be noted that only the first and last unit cells of the bipolar stack have positive and negative tabs. Because the tab resistance is calculated based on the current flow in the y-direction, but the voltage loss due to tab ohmic resistances is subtracted from the one-dimensional stack model in the z-direction, Eqs. 11 and 12 are approximated 1D in-plane resistances. However, as shown by the computed 2D effective resistance compared to the 1D in-plane resistance in Appendix B, the difference between the 2D effective resistance and the 1D in-plane resistance can be considered negligible.

One-dimensional parallel stack model.—Figure 3b shows the representative circuit diagram of the parallel stacking configuration of the single-layer cells. As the cells are arranged in parallel, all unit cells have the same voltage:

$$U_{stack,Par,OCV} = (\phi_{pos} - \phi_{neg}). \quad [13]$$

The current of the parallel stack can be described by the Kirchhoff's current law. For an ideal stack with a negligible cell-to-cell variation, the relationship between cell and stack current can be described as follow:

$$i_{cell} = \frac{i_{stack,Par}}{2N_{Par}}, \quad [14]$$

where N_{Par} is the number of unit cells stacked in parallel. The factor 2 indicates the double-coated configuration in each unit cell and is used to reproduce the experimental parallel stack measurements from Ito et al.[11] In real-world applications, a bipolar stack cannot be coated on both sides, whereas a double-coated configuration is often used for a parallel stack to reduce the gravimetric and volumetric contributions from inactive cell components.

Unlike a bipolar stack, each double-coated unit cell in a parallel stack has positive and negative tabs. While the cell voltage under load is identical, the sum of voltage loss due to positive and negative tabs must be subtracted using the stack current:

$$V_{stack,Par} = V_{cell} - i_{stack,Par} R_{tab,neg} - i_{stack,Par} R_{tab,pos}, \quad [15]$$

in which $R_{tab,neg}$ and $R_{tab,pos}$ are positive and negative tab resistance given by Eqs. 11 and 12. Then, the cell voltage, V_{cell} can be calculated as follows:

$$V_{cell} = (\phi_{pos} - \phi_{neg}) - i_{cell} R_{cell}, \quad [16]$$

where R_{cell} is the sum of ohmic resistances in a unit cell:

$$R_{cell} = R_{AM} + R_{CC,pos,eff} + R_{CC,neg,eff}. \quad [17]$$

Due to the characteristics of a two-dimensional current flow in the CC of the parallel stack (see Figs. 4b and B·3a in the Appendix), a separate two-dimensional electrical model is solved to calculate the effective resistance of the positive and negative CC ($R_{CC,pos,eff}$ and $R_{CC,neg,eff}$). In this 2D electrical model, we assume the potential drop in the CC to be small such that the current distribution across the CC remains uniform. The CC thickness in the middle of the stack is also halved to account for the double-coated configuration. Table B·III in the Appendix summarises the effective resistance computed using the 2D electrical model compared to the in-plane resistance calculated based on the resistivity and geometrical characteristics of the CC. The 1D in-plane resistance is found to be comparable to the 2D effective resistance, where the current boundary conditions are imposed on both sides of the CC.

Resistivity of electrode materials and current collectors.—In principle, resistivity is a fundamental intrinsic material property, measuring the strength of a material in opposing the flow of electric current with a uniform cross-sectional area. For a given material with an electronic conductivity, σ_i, the resistivity of the material, ρ_i can be represented by

$$\rho_{\mathrm{i}} = \frac{1}{\sigma_{\mathrm{i}}}. \quad [18]$$

Alternatively, the resistivity of a material can also be determined from

$$\rho_{\mathrm{i}} = \frac{R_{\mathrm{i}} A_{\mathrm{i}}}{L_{\mathrm{i}}}, \quad [19]$$

where R_i is the ohmic resistance of the material, A_i is the cross-sectional area and L_i is the length of the material. By rearranging Eq. 19, the ohmic resistance of different cell components i in the bipolar and parallel stack model can be estimated. While resistivity is a fundamental intrinsic material property, the definition of the surface area, A_i and length, L_i depend on the direction of the current flow, as shown in Fig. 4.

Besides the stack geometrical characteristics, the impacts of current flow on the ohmic resistance of BP and CC are also considered through the parameter—electronic conductivity. While metallic conductors such as aluminum and Li have an isotropic electronic conductivity, the effects of anisotropy can become dominant for materials such as carbon composite. Depending on the matrix and fiber alignments in a carbon composite, the through-plane electronic conductivity of carbon composites can be lower than the in-plane electronic conductivity by several orders of magnitude.[27–29] A parametric study was performed to assess the effects of different electronic conductivities of the carbon fiber BP on the gravimetric energy and power densities.

Two-dimensional thermal model.— *Energy balance.*—Chen et al.[30] have presented a detailed dimensional analysis of the conventional Li-ion thermal stack models by comparing the model accuracy and computational efficiency of the one-dimensional, two-dimensional and three-dimensional thermal models. The three-dimensional model is found to be most accurate, but the computational time is 3000–11000 times longer than the one-dimensional thermal model. They have shown that an in-plane two-dimensional model can capture the heat transfer behavior of the stack with good accuracy and efficiency. Based on this analysis, we have used a two-dimensional thermal model of the bipolar and parallel stacks, in which the heat generation is calculated from the one-dimensional electrochemical model. The heat transfer in the stack can be described by the following energy balance:[31]

$$\underbrace{\rho_{\mathrm{eff}} C_{\mathrm{p,eff}} \frac{\partial T}{\partial t}}_{\text{thermal energy storage}} = \underbrace{\frac{\partial}{\partial x}\left(k_{\mathrm{x}} \frac{\partial T}{\partial x}\right) + \frac{\partial}{\partial y}\left(k_{\mathrm{y}} \frac{\partial T}{\partial y}\right)}_{\text{in-plane heat conduction}} + \underbrace{Q_{\mathrm{gen,tot}}}_{\text{heat generation}} - \underbrace{Q_{\mathrm{conv}}}_{\text{convective heat dissipation}} - \underbrace{Q_{\mathrm{rad}}}_{\text{radiative heat dissipation}}, \quad [20]$$

where ρ_{eff} is the effective density of the stack, $C_{\mathrm{p,eff}}$ is the effective specific heat capacity of the stack at constant pressure, T is the temperature, k_{x} and k_{y} are the effective thermal conductivities in the x and y directions respectively. $Q_{\mathrm{gen,tot}}$ is the heat generation; Q_{conv} represents the heat dissipation by natural surface air convection and Q_{rad} denotes the heat dissipation by radiation. The effective in-plane thermal conductivity ($k_{\mathrm{eff}} = k_{\mathrm{x}} = k_{\mathrm{y}}$) can be calculated as[32]

$$k_{\mathrm{eff}} = \frac{\sum_{i=1}^{N_{\mathrm{cell}}} v_{\mathrm{i}} k_{\mathrm{i}}}{v_{\mathrm{cell}}}, \quad [21]$$

where N_{cell} is the number of cell components in each unit cell, v_i/v_{cell} is the volume fraction and k_i is the thermal conductivity of each component. Equation 21 is derived assuming an ideal parallel conduction without interfacial thermal resistance in each of the coplanar layers, which is only exact if the through-thickness is uniform.

For a parallel stack with the same layer-to-layer surface area across the stack, the effective thermal conductivity is given by[20]

$$k_{\mathrm{eff,Par}} = \frac{1}{d_{\mathrm{cell,Par}}}(d_{\mathrm{CC,pos}} k_{\mathrm{CC,pos}} + d_{\mathrm{CC,neg}} k_{\mathrm{CC,neg}} + 2d_{\mathrm{pos}} k_{\mathrm{pos}} + 2d_{\mathrm{neg}} k_{\mathrm{neg}} + 2d_{\mathrm{elec}} k_{\mathrm{elec}}), \quad [22]$$

where $d_{\mathrm{cell,Par}}$ is the thickness of the cell ($d_{\mathrm{cell,Par}} = d_{\mathrm{CC,pos}} + d_{\mathrm{CC,neg}} + 2d_{\mathrm{pos}} + 2d_{\mathrm{neg}} + 2d_{\mathrm{elec}}$). $d_{\mathrm{CC,pos}}$ and $k_{\mathrm{CC,pos}}$ are the thickness and thermal conductivity of the positive CC; $d_{\mathrm{CC,neg}}$ and $k_{\mathrm{CC,neg}}$ are the thickness and thermal conductivity of the negative CC; d_{pos} and k_{pos} are the thickness and thermal conductivity of the PE, d_{neg} and k_{neg} are the thickness and thermal conductivity of the NE; d_{elec} and k_{elec} are the thickness and thermal conductivity of the SE.

To date, only Xu et al.[33] have measured the cross-plane thermal conductivity of the LiPON SE. In conventional liquid-based Li-ion batteries, Maleki et al. showed that the in-plane thermal conductivity can be larger than the cross-plane thermal conductivity by a factor between 6–13.[34] Therefore, a parametric study was performed to analyze the effects of using different SEs thermal conductivities on the surface temperature of both stacks (see Fig. B·4d in Appendix B). Due to dominant thermal conductivities from other cell components, the effects of using different SEs thermal conductivities on the stack average surface temperature were found to be negligible.

Similarly, the effective in-plane thermal conductivity of a bipolar stack can be estimated by

$$k_{\mathrm{eff,BP}} = \frac{1}{d_{\mathrm{cell,BP}}}(d_{\mathrm{BP}} k_{\mathrm{BP}} + d_{\mathrm{pos}} k_{\mathrm{pos}} + d_{\mathrm{neg}} k_{\mathrm{neg}} + d_{\mathrm{elec}} k_{\mathrm{elec}}), \quad [23]$$

in which $d_{\mathrm{cell,BP}}$ is the thickness of the bipolar unit cell ($d_{\mathrm{cell,BP}} = d_{\mathrm{pos}} + d_{\mathrm{elec}} + d_{\mathrm{neg}} + d_{\mathrm{BP}}$); d_{BP} and k_{BP} are the thickness and thermal conductivity of the BP.

The density, ρ_{eff}, and specific heat capacity, $C_{\mathrm{p,eff}}$, of the stacks can be estimated as:[30]

$$\rho_{\mathrm{eff}} C_{\mathrm{p,eff}} = \frac{\sum_{i=1}^{N_{\mathrm{cell}}} v_{\mathrm{i}} \rho_{\mathrm{i}} C_{\mathrm{p,i}}}{v_{\mathrm{cell}}}, \quad [24]$$

where ρ_{i} and $C_{\mathrm{p,i}}$ are the density and specific heat capacity of each component layer of the cell. Mei et al.[35] had calculated the effective specific heat capacity of the cell by defining the volume average of a mass-based property. If the effective density and specific heat capacity from Eq. 24 need to be calculated separately, a mass average instead of a volume average should be used, as shown by

$$C_{\mathrm{p,eff}} = \frac{\sum_{i=1}^{N_{\mathrm{cell}}} m_{\mathrm{i}} C_{\mathrm{p,i}}}{m_{\mathrm{cell}}}, \quad [25]$$

where m_i is the mass of each cell component and m_{cell} is the total mass of the cell.

Calculation of heat generations.—Generally, the heat generation in a battery, $Q_{\mathrm{gen,tot}}$ can occur irreversibly (Q_{irrev}) and reversibly (Q_{rev}):

$$Q_{\mathrm{gen,tot}} = Q_{\mathrm{irrev}} + Q_{\mathrm{rev}}. \quad [26]$$

In an all-solid-state Li-metal stack, the irreversible heat generation, Q_{irrev} can be attributed to losses due to the ionic transport in the SE (Q_{ohm}), reaction current at the electrolyte-electrode interface

($Q_{neg/pos}$), solid Li transport in the non-porous bulk PE (Q_{diff}) and electronic transport in the active materials and CC (Q_{CC}):

$$Q_{irrev,stack,BP/Par} = I_{stack,BP/Par}(\eta_{ohm} + \eta_{neg} + \eta_{pos} + \eta_{diff}) + I^2_{stack,BP/Par}R_{ohm,BP/Par}, \quad [27]$$

where η_{ohm} is the ohmic overpotential in the SE; η_{neg} and η_{pos} are the charge transfer overpotentials due to interfacial reaction kinetics at the respective interface; η_{diff} is the solid diffusion overpotential. The expressions to calculate these overpotentials can be found in Appendix A. The total thickness of both stacks is calculated from the sum of the stack thickness, the estimated volume change due to Li metal and the thickness of the pouch (see Table B·II in Appendix B). The tab thickness is estimated based on literature values from Zhao et al.[36] and Hales et al.[37]

For a bipolar stack, $R_{ohm,BP}$ is the sum of ohmic resistances of the active materials and BP in a bipolar stack ($R_{ohm,BP} = R_{AM} + R_{BP}$). On the other hand, $R_{ohm,Par}$ is the sum of ohmic resistances of the active materials and CC in a parallel stack ($R_{ohm,Par} = R_{AM} + R_{CC}$). The irreversible heat dissipation due to Joule heating at both tabs, $Q_{irrev,tab}$ can be calculated by

$$Q_{irrev,tab,BP/Par} = I^2_{stack,BP/Par}R_{tab,BP/Par}, \quad [28]$$

in which $R_{tab,BP/Par}$ is the ohmic resistance of both tabs in the bipolar and parallel stack.

The reversible heat generation, Q_{rev} occurs due to structural change of the PE and can be calculated as follows:[38]

$$Q_{rev,stack,BP/Par} = \frac{I_{stack,BP/Par}\overline{T}\Delta S}{nF}, \quad [29]$$

where n is the number of electrons and ΔS is the entropy of the stack, which can be estimated experimentally from the entropic heat coefficient.

Thermal boundary conditions.—The convective heat dissipation in the two-dimensional thermal model can be defined as[32]

$$q_{conv} = \left[\frac{1}{h} + \frac{d_{pouch}}{k_{pouch}}\right]^{-1}(T_{amb} - T), \quad [30]$$

in which h is the heat transfer coefficient ($h = 5\ W\ m^{-2}\ K^{-1}$), d_{pouch} and k_{pouch} are the thickness and thermal conductivity of the pouch. The initial condition is given by the operating temperature and the ambient temperature is defined as 20 °C. By multiplying with the stack surface area, q_{conv} can be converted to Q_{conv} ($Q_{conv} = q_{conv} \times A_{ref}$). Both stacks were cooled by natural air convection across the top surface of the stacks.

The parallel stack in the works of Ito et al.[11] was vacuum-sealed inside a laminated aluminum pouch. We consider the same material for both bipolar and parallel pouches in this work. Considering the surface emissivity of the laminated aluminum pouch, the radiative heat dissipation from the top and bottom of each pouch, Q_{rad} can be estimated by[30]

$$Q_{rad} = \epsilon_{Al,top}\sigma_{Boltz}(T^4_{amb,top} - T^4) + \epsilon_{Al,down}\sigma_{Boltz}(T^4_{amb,down} - T^4), \quad [31]$$

where ϵ_{Al} is the surface emissivity of aluminum ($\epsilon_{Al,top} = \epsilon_{Al,down} = 0.09$) and σ_{Boltz} is the Stefan-Boltzmann's constant ($\sigma_{Boltz} = 5.67 \times 10^{-8}\ W\ m^{-2}\ K^{-4}$). Because the internal architecture of the stack is opaque, the radiative heat dissipation inside the stack is negligible.[30]

Electrochemical-thermal coupling.—The heat generation in the thermal model was calculated from the electrochemical model, whereas the physical parameters in the electrochemical model were modified to include the temperature dependence, therefore coupling the electrochemical model to the thermal model two-ways. We use the notation $\overline{T}$ in our one-dimensional electrochemical model to represent the surface-averaged temperature evaluated from the two-dimensional model:

$$\overline{T} = \frac{1}{A}\iint T dA. \quad [32]$$

The system of DAEs were solved in COMSOL Multiphysics ® V5.4. A summary of the model parameters is given in Table I.

Experimental Parameterisation

A similar parameterisation procedure and the testing rig is used as in Offer et al.[13] The temperature was controlled with the Peltier element and measured with the thermocouples type K. The corresponding voltage and impedance profiles of the STMicroelectronic cell were recorded with Gamry Interface 1000. Potentiostatic Electrochemical Impedance Spectroscopy (PEIS) measurements at the open-circuit voltage of each pulse were taken at 25 °C, 35 °C, 45 °C and 55 °C to extract two of the temperature-dependent model parameters: the ionic conductivity in the SE and the exchange current densities at the NE and SE interface. The estimation of the temperature-dependent diffusion coefficient in the non-porous PE is first discussed, followed by the measurement of the entropic heat coefficient.

Figure 5a shows the PEIS measurements at the four surface controlled temperatures. The ionic conductivity and charge transfer at both interfaces change marginally with SOC within the voltage window of 3.0 V and 4.2 V under isothermal operating conditions.[13] However, as the temperatures increase, the electrolyte resistance decreases from 72.56 Ω cm^2 to 6.71 Ω cm^2. The charge transfer resistances at the NE and PE also decrease from 18.27 Ω cm^2 and 52.42 Ω cm^2 to 0.75 Ω cm^2 and 3 Ω cm^2, respectively.

The Distribution Function of Relaxation Times (DRT) analysis is used to distinguish the various contributions to the voltage loss at different operating temperatures.[43] The DRT analysis reveals four polarization peaks at 25 °C and three peaks at 35 °C, at 45 °C and at 55 °C. A small shift in the DRT peaks is observed with increasing temperatures. Due to the different PEIS signals observed in this work compared to the PEIS measured in Refs. 13, 39, 44 a log-normal statistical analysis was used to quantify this variability by measuring the initial cell impedance of 23 cells after the formation cycling (three cycles of constant-current charge and discharge) at ambient temperatures (see Appendix A).

Two sets of parameters were estimated from the PEIS measurements: the ionic conductivity of the SE, σ_{elec} and the exchange current density, $i_{0,neg}$. The temperature-dependence of these parameters can be described by Arrhenius expressions:[45]

$$\sigma_{elec} = \sigma_{elec,ref}\exp\left[-\frac{E_{a,elec}}{R_{gas}}\left(\frac{1}{T} - \frac{1}{T_{ref}}\right)\right], \quad [33]$$

$$i_{0,neg} = i_{0,neg,ref}\exp\left[-\frac{E_{a,i0}}{R_{gas}}\left(\frac{1}{T} - \frac{1}{T_{ref}}\right)\right], \quad [34]$$

where $\sigma_{elec,ref}$ and $i_{0,neg,ref}$ are the ionic conductivity and exchange current density measured at the reference temperature, E_a is the activation energy and T_{ref} is the reference temperature defined as 298.15 K. Figures 5c and 5d show a good fit.

The temperature-dependent OCP can be described by

$$U_{cell}(T) = U_{cell,ref} + (T - T_{ref})\frac{\partial U(x_{Li})}{\partial T}, \quad [35]$$

where $U_{cell,ref}$ is the OCP at 25 °C and $\partial U(x_{Li})/\partial T$ is the experimentally measured entropic heat coefficient.

Table I. Summary of stack geometrical and thermal parameters.

Parameters	Positive electrode ($LiCoO_2$)	Solid electrolyte (LiPON)	Negative electrode/Current collector (Li)	References
Thickness, d	6 μm	2 μm	10 μm	7, 39
Surface area, A_{ref}	0.0244 m^2	0.0244 m^2	0.0244 m^2	20
Density, ρ	3121 kg m^{-3}	2680 kg m^{-3}	534 kg m^{-3}	32–34
Electronic conductivity, σ	3100 S m^{-1}	—	1.1×10^7 S m^{-1}	40, 41
Thermal conductivity, k	53.6 W m^{-1} K^{-1} (in-plane)	1.4 W m^{-1} K^{-1}	81.8 W m^{-1} K^{-1}	32, 33, 42
Specific heat capacity, C_p	602 J kg^{-1} K^{-1}	1400 J kg^{-1} K^{-1}	3582 J kg^{-1} K^{-1}	32–34
Parameters	Aluminium bipolar plate/Current collector	Aluminium tab	Copper tab	References
Thickness, d	10 μm	10 μm	10 μm	7
Surface area, A_{ref}	0.0244 m^2	7×10^{-4} m^2	7×10^{-4} m^2	17, 20
Tab distance from the edge, d_{edge}	—	3×10^{-3} m	3×10^{-3} m	17
Tab thickness, d_{tab}	—	0.2 mm	0.2 mm	36, 37
Density, ρ	2700 kg m^{-3}	2700 kg m^{-3}	8960 kg m^{-3}	32
Electronic conductivity, σ	3.78×10^7 S m^{-1}	3.78×10^7 S m^{-1}	5.96×10^7 S m^{-1}	20, 41
Thermal conductivity, k	238 W m^{-1} K^{-1}	238 W m^{-1} K^{-1}	398 W m^{-1} K^{-1}	20, 32
Specific heat capacity, C_p	897 J kg^{-1} K^{-1}	897 J kg^{-1} K^{-1}	385 J kg^{-1} K^{-1}	32

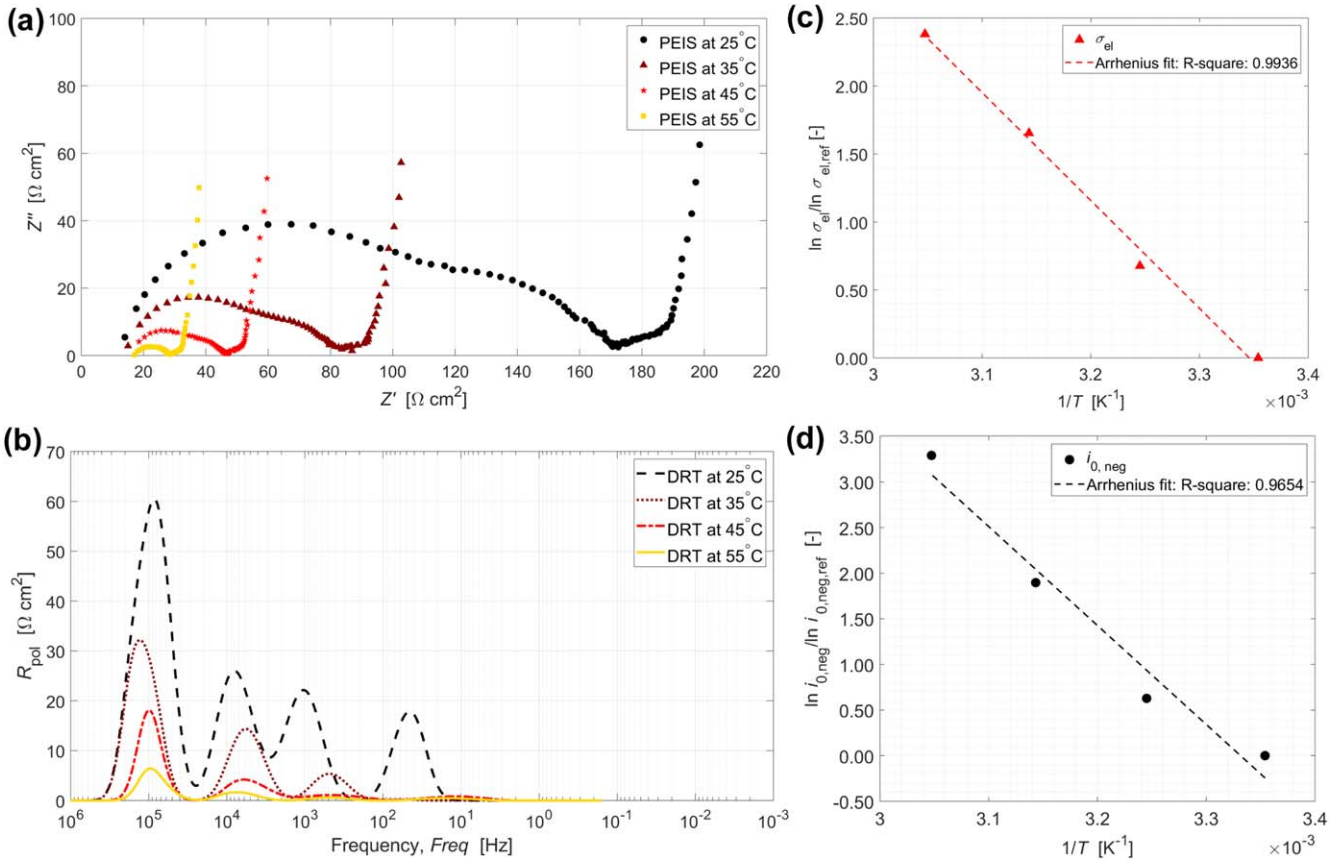


Figure 5. Experimentally measured cell impedance at four surface controlled temperatures: (a) An increase in the temperature from 25 °C to 55 °C reduces the electrolyte resistance by a factor of 10, the charge transfer resistance at the Li|LiPON interface by a factor of 24 and the charge transfer resistance at the LiPON|$LiCoO_2$interface by a factor of 17. (b) Corresponding DRT profiles. (c) The ionic conductivity estimated based on PEIS measurements obey the Arrhenius relationship ($R^2 = 0.9936$). (d) The temperature-dependent exchange current density at the Li|LiPON interface can also be described with the Arrhenius relation ($R^2 = 0.9654$).

Measurement of temperature-dependent diffusion coefficients in the positive electrode.—Concentration-dependent diffusion coefficients at 25 °C, 35 °C, 45 °C and 55 °C were obtained from the GITT data, following the procedures in Ref. 13. Figure 6a shows the concentration and temperature-dependent diffusion coefficients. For high SOCs, temperature does not affect the diffusion coefficients significantly. At low SOCs, the Li concentration in the PE increases, and an increase in the diffusion coefficient of a factor of 50 can be observed when the operating temperatures increases from 25 °C to 55 °C. The increase in the operating temperature reduces the mass transport barrier in the PE for low SOCs. The concentration and temperature-dependent diffusion coefficient can be approximated by

$$D_{\mathrm{Li}} = D_{\mathrm{Li,25\,^\circ C}}(x_{\mathrm{Li}}) \times \exp\left[-\frac{E_{\mathrm{a,diff}}}{R_{\mathrm{gas}}}\left(\frac{1}{T} - \frac{1}{T_{\mathrm{ref}}}\right)\right], \quad [36]$$

where $E_{\mathrm{a,diff}}$ is an estimated activation energy ($E_{\mathrm{a,diff}} = 20000\ \mathrm{J\ mol^{-1}}$). The comparison of the approximated function to the experimental measurements is given in Appendix A.

Measurement of entropy as a function of concentrations.—Entropy is a measure of the Li atoms orderings and phase change in the electrodes during charge and discharge.[46,47] The insertion of Li atoms into the lattice of the PE induces structural change and increases the disorder of atoms on the lattice. The entropy change under discharge must be identically opposite (negative in value) compared to its value under charge.[46]

The entropy, ΔS is proportional to the entropic heat coefficient, $\partial U(x_{\mathrm{Li}})/\partial T$ as follows[47]:

$$\Delta S = \left[nF\frac{\partial U(x_{\mathrm{Li}})}{\partial T}\right]_{\mathrm{SOC,p}}, \quad [37]$$

where n is the number of electrons and F is the Faraday's constant ($F = 96,485\ \mathrm{C\ mol^{-1}}$). ΔS is determined with the potentiometric method by measuring the change of OCP with respect to temperature at a fixed SOC. This method is preferred to the calorimetric method for thermally thin cell.[46] Zhang et al. have proposed a discontinuous measurement with a shortened voltage relaxation time to approximate the entropic heat coefficient ($\approx \partial U(x_{\mathrm{Li}})/\partial T$). Nevertheless, a relative error of 2% compared to the full discontinuous measurement method requiring long voltage relaxation was reported with this method in the temperature range between 20 °C and 30 °C.[47] As the temperature window in this model ranges from 25 °C to 55 °C, the full discontinuous measurement of $\partial U(x_{\mathrm{Li}})/\partial T$ was used to minimize this uncertainty.

Thomas et al.[46] have developed experimental procedures to measure the entropic heat coefficient for a temperature range between 21 °C and 29 °C. These procedures were adapted in this work for a wider temperature range from 25 °C to 55 °C. The cell was first charged with a constant current of 1 mA to 4.2 V at 25 °C and then held at the constant voltage of 4.2 V until the current dropped to 0.1 mA. Then, the cell was rested for 30 min before being discharged with C/10 until 5% of the nominal capacity is removed. A step-like temperature profile of 25 °C, 35 °C, 45 °C and 55 °C was

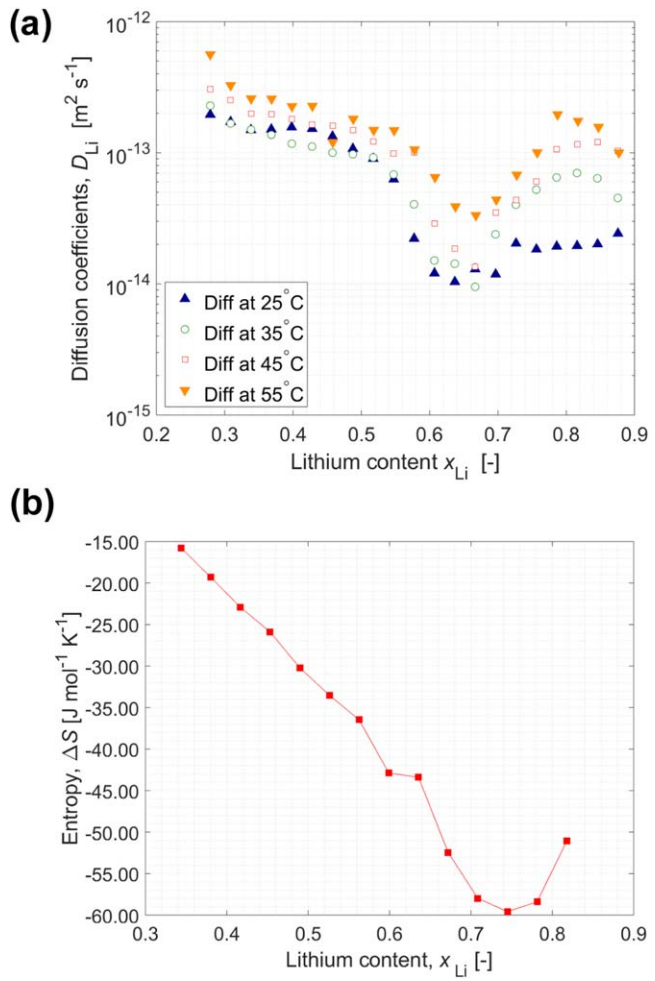


Figure 6. (a) Experimentally measured solid diffusion in the PE at four different operating temperatures: The impact of higher operating temperature improves the solid diffusion for low SOCs. (b) Entropy of reaction in the $LiCoO_2$measured between 95% and 25% SOC.

applied to the cell, during which the cell was allowed to relax for 3 h before each temperature change. The experimental procedures were repeated to remove an incremental 5% of the cell's initial capacity until the SOC reached 25%. The overpotential of the cell for SOCs smaller than 25% is so dominant such that the OCP of the cell continues to change even after 10 h of relaxation per temperature. Therefore, the entropic heat coefficient was measured for the SOC window between 95% and 25%. Figure 6b shows the experimental estimated entropy of reaction in the non-porous bulk $LiCoO_2$ electrode. The entropy of reaction becomes more negative with decreasing SOCs, which can be attributed to increasing lattice disorders.[46]

Model Qualitative Validations

Figure 7a shows the simulated and the experimentally measured voltage profile for current discharged at a cell temperature of 25 °C, 35 °C, 45 °C and 55 °C. While most model parameters were estimated from experimental measurements, k_{pos} was used as a fitting parameter in this work, which is given in Appendix A. As shown by Fig. 7a, the cell performance improves with increasing operating temperatures, which can be attributed to the decreasing electrolyte and interfacial impedance (Fig. 5) as well as higher diffusion coefficients (Fig. 6a). The single-unit cell model was then scaled up by adjusting the electrode active surface area. The scaled cell model was placed in series and in parallel to achieve bipolar and parallel stack configurations.

Toyota[9] showed that the bipolar stack could output a stack voltage of 16.26 V (indicated by the red star in Fig. 7b). Four single-layer scaled cells were stacked in series giving a predicted maximum output voltage of 16.45 V, close to that achieved by Toyota on a four-layer all-solid-state stack using $LiCoO_2$as the PE, sulfide as the SE and graphite as the NE.

Ito et al.[11] have developed a parallel stack with the nominal capacity of approximately 1 Ah by stacking three single-layer double-coated cells in parallel. The electrochemical cell had a Li_2O-ZrO_2 coated $LiNi_{0.8}Co_{0.15}Al_{0.05}O2$ (NCA) PE, sulfide-based SE and graphite NE. Figures 7c and 7d compare qualitatively the model predicted parallel stack profile with their experimental stack result. The single-cell model in Fig. 7c uses a factor of 1 instead of 2 in Eq. 14 and $N_{Par} = 1$, whereas the double-coated single-cell model retains the factor of 2 in Eq. 14. N_{Par} is changed to three for the third discharge curve to model the three-layers parallel configuration.

Model-Based Stack Design

Bipolar and parallel stack discharge.—EiG C020 is chosen as the reference in the stack design of this work. The PE of the EiG C020 cell is 70 μm and the stack excluding the pouch case is 7.074 mm thick.[20] In solid-state Li-metal cells, the thickness of a non-porous PE is limited by the slow diffusion of intercalated Li-ions, thus indicating a thinner PE would be used.[13] Moreover, instead of graphite, Li is used as the NE. Therefore, the overall stack thickness assumed for this study is 0.1769 cm. Within the same stack volume for both bipolar and parallel stacks, the thickness of each component of the single unit cell was fixed, with values as given in Table I. Therefore, the stack volume corresponds to 32 double-coated parallel cells or 63 cells in a bipolar configuration. Figures 8b and 8c show the simulated discharge stack profile for both bipolar and parallel configurations. As shown by Fig. 8b, the bipolar stack can achieve a stack voltage up to 265 V with a stack capacity of 0.7 Ah, whereas the capacity of the parallel stack is 23 Ah, at a C-rate of 0.2 C.

Two common degradation mechanisms associated with the use of Li metal have been observed experimentally: (1) Li creep and (2) voids formation at the interface between the NE and the SE.[48–51] Due to the low melting point and high homologous temperatures of Li metal between 25 °C and 55 °C, Li exhibits a strong temperature-dependent creep and volume deformation.[48] An unrestrained Li creep could flow through the pores and grain boundaries of the SE to cause an eventual internal short-circuit against the PE.[49,51] As a result, an external stack pressure is required to restrict the internal volume deformation due to Li metal.[48–51] Zhang et al.[52] have developed an in situ instrument to track the volume change of Li metal electrode during lithiation and delithiation. They showed that a thickness change up to 23 μm is observed during cycling, even when the cell was placed under an external pressure of 850 kPa. Li et al.[53] proposed the use of polyurethane foam as a spacer (range of thickness <3.5 mm) to reduce the internal stress and strain inside the pouch of large-format Li-ion batteries. Based on the experimental observations of Ref. 52, it was inferred that a commercial large-format solid-state Li-metal stack could include internal spacers. By multiplying the total number of Li NEs and CC with the thickness change observed by Ref. 52, a spacer made of polyurethane foam of thickness 2.231 mm (parallel) and 1.426 mm (bipolar) between the stack and the pouch layer was included in this study. Therefore, the bipolar and parallel stacks have a projected volume of 84.06 cm^3 and 102.71 cm^3 respectively. As shown by Fig. B·1 in Appendix B, the additional spacer decreases the gravimetric energy density by less than 5% for parallel and bipolar stacks due to the low density of the polyurethane (35–40 kg m^{-3}).[53] However, the polyurethane spacer can account for 43%–53% of the stack volume (see Fig. B·1 in Appendix B) if the spacer occupied the entire space between the stack and pouch. Table B·II shows an example calculation of the mass and volume of a parallel stack that uses Li as the negative CC and bipolar stack that

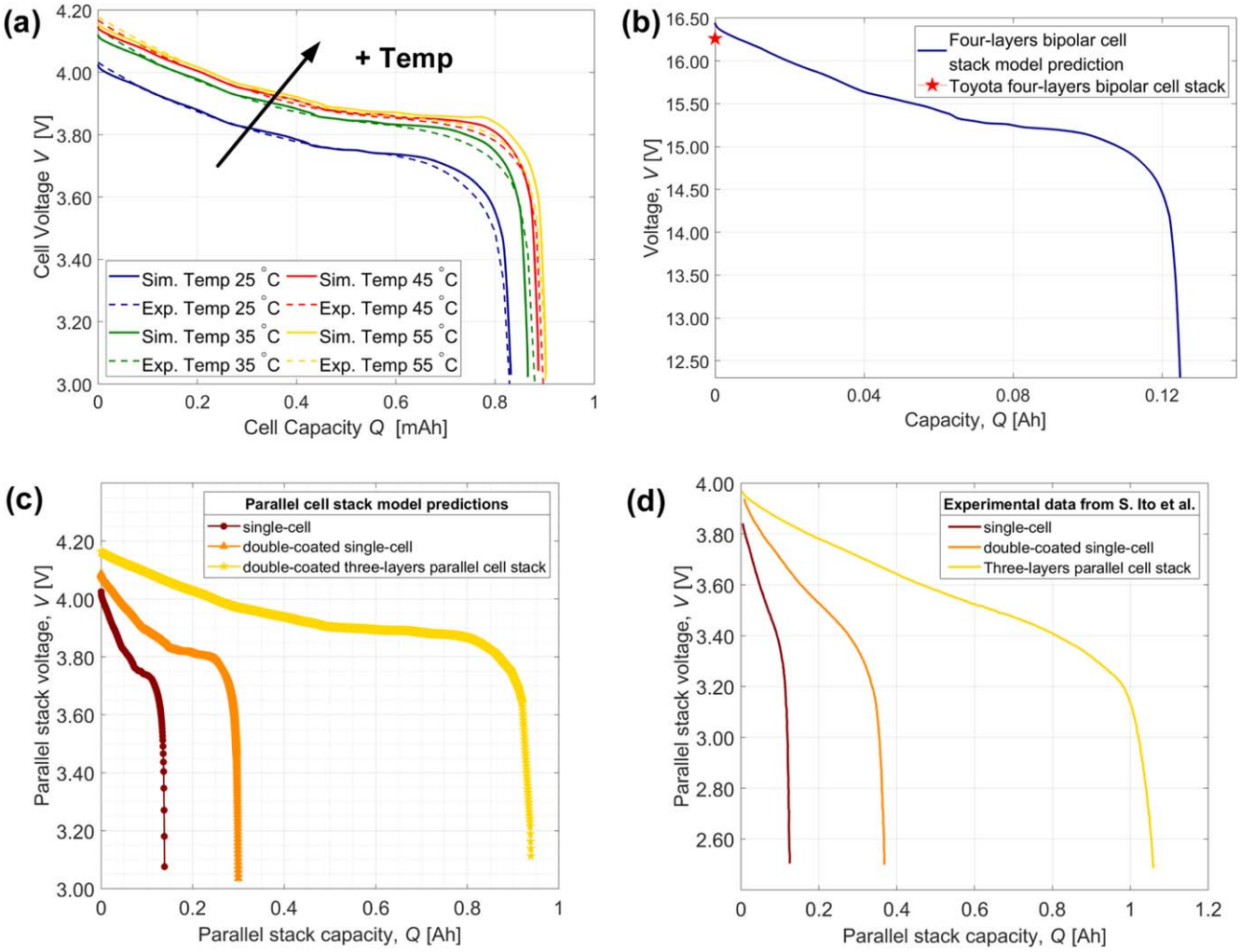


Figure 7. (a) Comparison of simulated constant-current discharge profiles of the single-unit cell model to experimental measurements at four different operating temperatures. (b) Qualitative validation of simulated bipolar stack voltage profile (4 cells) with the maximum experimental stack output voltage from Toyota.[9] Terminal voltage for a 0.1C discharge from the single-cell, double-coated single-cell and 3-cell parallel stack, (c) as predicted by the model and (d) obtained experimentally from Ito et al.[11]

uses aluminum as the BP. The calculated stack volume and mass for different CC and BP materials are summarised in Table II.

Volumetric and gravimetric density.—With known mass and volume of the stacks, the energy and power densities of the stacks can be estimated. Figures 9a and 9b show the simulated Ragone profiles of bipolar and parallel stacks compared to Sanyo 18 650 Li-ion,[54] Sanyo prismatic Li-ion,[54] Li-sulfur[55] and supercapacitor LTO/LCO.[56] It should be noted that a typical Ragone profile comparing the power and energy density of different cell chemistries is C-rate dependent. The Ragone plots for bipolar and parallel stacks in this work were simulated with the discharge C-rates from 0.1 C to 5 C. 1C corresponds to 0.15 A for the bipolar stack and 9.6 A for the double-coated parallel stack. For a C-rate of 0.1, the volumetric energy density can reach up to 447.9 Wh L^{-1} for the parallel stack using Li as the negative CC (denoted as parallel Li stack) and 908 Wh L^{-1} for the bipolar stack using aluminum BP (denoted as a bipolar aluminum stack). For stacks with polyurethane spacers, the bipolar aluminum stack has a higher volumetric energy density than a parallel copper stack and parallel Li stack. As shown in Fig. 8, the bipolar stack is a relatively high-power cell with a discharge stack voltage of up to 265 V. As a result, the volumetric energy density of the bipolar aluminum stack is approximately two times higher than that of the parallel copper stack. The parallel copper stack has higher volumetric energy and power density than the parallel Li stack due to the Li volume deformation inside the stack. If Li foil is used as the negative CC, the total thickness change due to Li CC and NEs can reach up to 2.231 mm. As a result, 53 vol-% of the spacer is required to reduce the internal stress and strain, however, because of the density of copper (8.960 g cm^{-3}) compared to Li (0.534 g cm^{-3}), the parallel Li stack has higher gravimetric energy and power density than the parallel copper stack. If copper foils substitute Li CC, the volume fraction of the spacer can be reduced from 53% to 43%, but the mass ratio of the CC increases from 33% to 62%. Figure B·1 in Appendix B illustrates the mass and volume fraction of the parallel Li and bipolar aluminum stack.

For an ideal stack without the volume deformation due to Li electrodes and CC, the volumetric power and energy density of bipolar aluminum stack without a spacer can be 1.71 times higher than that of the bipolar aluminum stack with a spacer. Similarly, the volumetric power and energy density of parallel Li stack without a spacer can be higher than the parallel Li stack with a spacer by a factor of 2.13.

The maximum volumetric energy density of parallel Li stack is 1.81 higher than the maximum of Sanyo 18 650 Li-ion cylindrical cell, 3.05 times higher than the maximum of Li-sulfur reported by Mikhaylik,[55] 6.72 times higher than the maximum of LTO/LCO supercapacitor reported by DuPasquier et al.[56] Likewise, a factor of 3.68, 6.18 and 13.61 can be obtained with the bipolar aluminum stack. In a parallel stack using Li as both the NEs and the negative

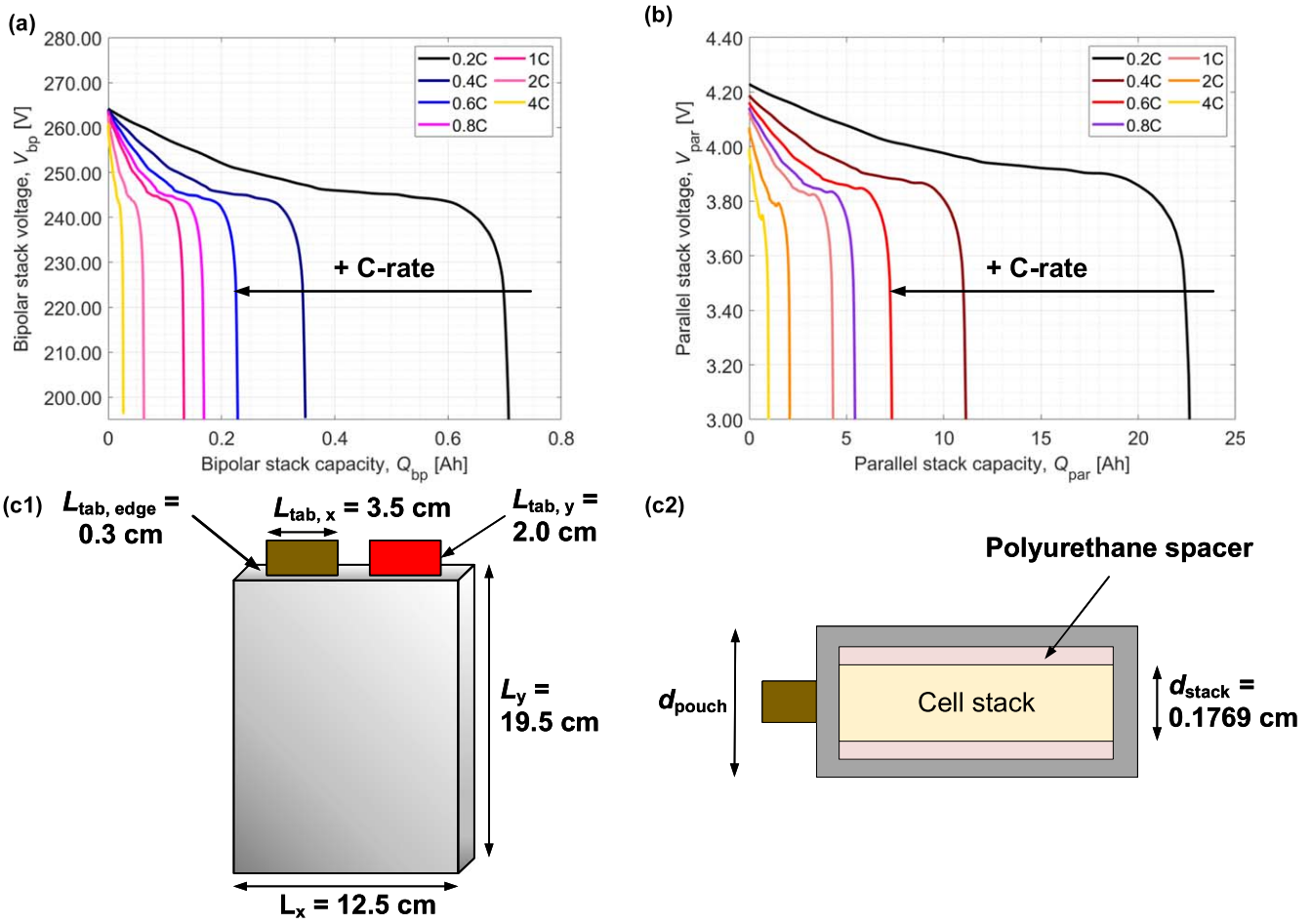


Figure 8. (a) With 63 cells stacked in series, a bipolar stack can achieve up to 265 V with a limited stack capacity of less than 1 Ah. (b) In a parallel stack, a high capacity of about 23 Ah can be obtained at a C-rate of 0.2 C with a maximum stack voltage of 4.2 V. (c1) The external dimensions of the pouch and tabs. (c2) Thickness of the pouch includes the stack thickness and the thickness of the polyurethane spacer used to reduce the internal volume deformation due to Li creep.

Table II. Calculated stack mass and volume for different parallel and bipolar stacks.

Parallel stack		
Materials	Stack mass (g)	Stack volume (cm^3)
Lithium foil	86.499	102.708
Copper foil	153.629	84.208
Bipolar stack		
Carbon fibres	89.047	84.064
Aluminium foil	102.378	84.064
Titanium foil	130.216	84.064
Stainless steel	181.365	84.064

CC, due to the higher specific capacity of Li (3860 mAh g^{-1}) compared to graphite NE (372 mAh g^{-1}), the maximum gravimetric energy density of the parallel Li stack can be 4.95 times higher than Sanyo 18 650 Li-ion cylindrical cell. However, if Li is used as the NE and copper is used as the CC, this comparative factor reduces to 2.79. On the other hand, the maximum gravimetric energy density of the bipolar aluminum stack can be 6.93 times higher than Sanyo 18 650 Li-ion cylindrical cell.

When the discharge C-rate increases, the energy density decreases but the power density increases. Only 83.39 Wh L^{-1} and 68.48 Wh kg^{-1} can be achieved with the bipolar aluminum stack and 36.78 Wh L^{-1} and 43.67 Wh kg^{-1} with the parallel Li stack when the stacks were discharged with 1C. The estimated volumetric and gravimetric power density at 1C for the bipolar aluminum stack are 439.21 W L^{-1} and 360.64 W kg^{-1}, respectively. Similarly, for the parallel Li stack, the corresponding volumetric and gravimetric power density are 360.8 W L^{-1} and 428.41 W kg^{-1}. The low energy density at 1C can be attributed to the limited thickness of the PE in each unit cell of the stack. For a non-porous PE, the increase in the thickness is limited by the slow diffusion in the electrode.[13] As a result, the active materials only account for 27% to 33% of the parallel and bipolar volume ratio. Also, the volumetric energy density was significantly affected by the possible volume deformation of Li. For an ideal scenario without deformation, the estimated volumetric energy density for the parallel Li and bipolar aluminum stack at 1C is 78.17 Wh L^{-1} and 142.19 Wh L^{-1} respectively. The maximum volumetric and gravimetric power density for bipolar aluminum stack at 5C is 2198 W L^{-1} and 1805 W kg^{-1}, which is close to the maximum volumetric and gravimetric power density for LTO/LCO supercapacitor (2608 W L^{-1}, 1860 W kg^{-1}) reported by DuPasquier and co-workers.[56] Finally, we note that this is a general electrochemical-thermal model that does not consider the impact of any stack failure such as internal short-circuit due to the propagation of Li filaments.

The effects of current collectors.—The materials of the CC have a significant impact on the gravimetric power and energy density of the stack. Four different materials are investigated in this work as potential BP for large-format bipolar solid-state Li-metal stacks,

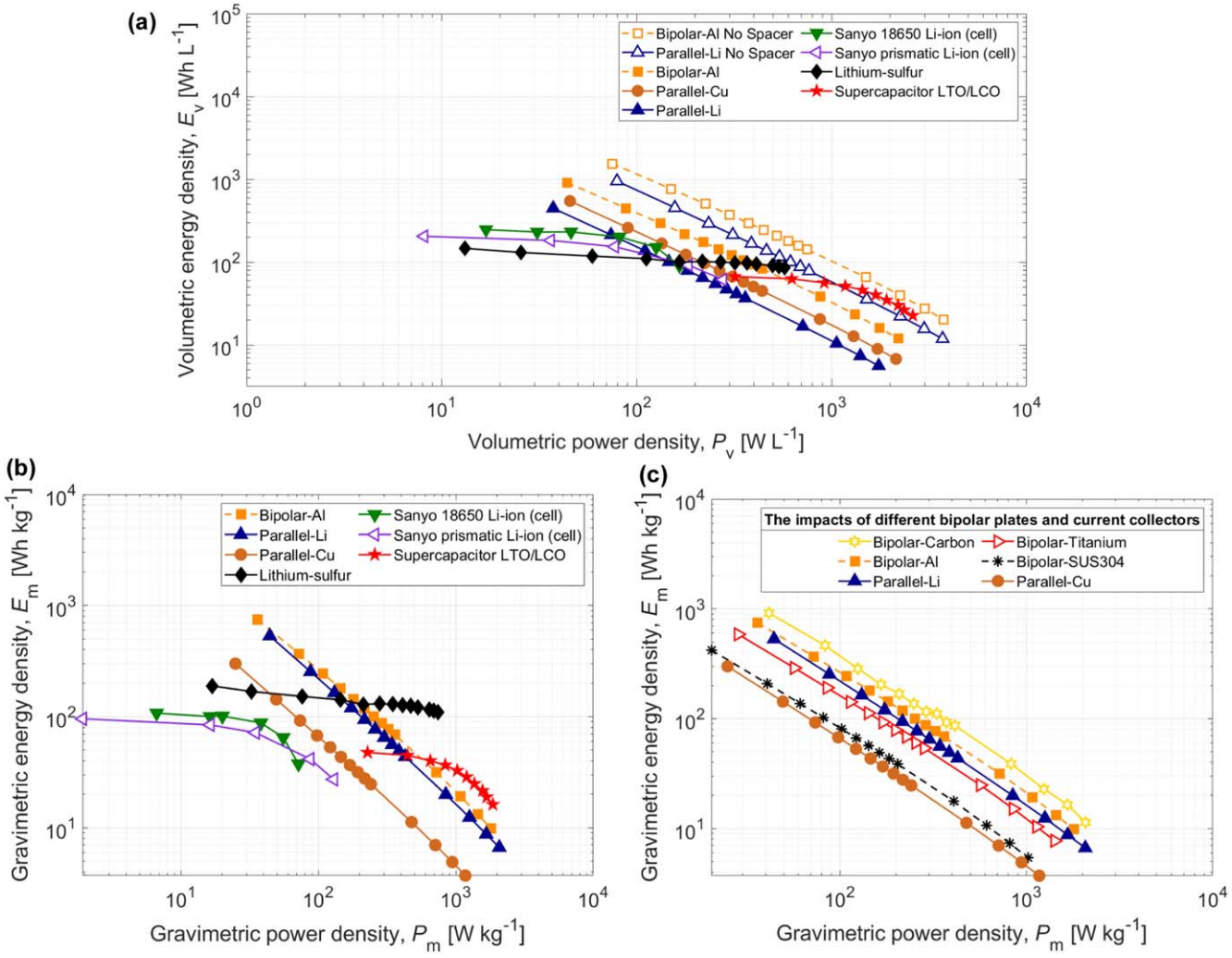


Figure 9. (a) Comparison of simulated volumetric Ragone profiles of bipolar and parallel stack with aluminum BP (orange square), copper foils (brown circle) and lithium foils (blue triangle) and without polyurethane spacer to Sanyo 18 650 lithium-ion (cell),[54] Sanyo prismatic lithium-ion (cell),[54] lithium-sulfur[55] and supercapacitor LTO/LCO.[56] (b) Simulated gravimetric Ragone profiles of bipolar and parallel stacks compared to literature values. (c) Comparison of the gravimetric energy and power density of bipolar and parallel stacks made up of different types of CC: carbon composite, aluminum foils, lithium foils, titanium foils, SUS304 stainless steel foils and copper foils.

which include aluminum foil, titanium foil, carbon composite and SUS stainless steel. As for large-format parallel solid-state stacks, copper and Li foils as negative CC are compared in this study.

Liu et al.[19] have demonstrated that aluminum foil is stable as a BP material for sodium-ion cells. Aluminium foil is shown to exhibit a negligible parasitic current from 0 V to 5 V, while copper foil shows a sharp rise in current density from 3.6 V onwards, due to copper oxidation at high potentials. They also demonstrated that there is no alloying reaction between aluminum foil and the metallic sodium. In a separate study led by Fraunhofer IKTS, Wolter et al.[21] used the aluminum foil as the BP in a Li-based bipolar stack and showed that a stack voltage up to 9 V can be achieved with four unit cells. LaFollette and Utah[18] proposed a composite of long carbon fibres filled with carbon particles and fluoroelastomer as the BP for lead-acid batteries.

Due to the density of the carbon composite (1.82 g cm^{-3})[18] compared to aluminum foil (2.70 g cm^{-3}),[32] a gain factor up to 1.15 and 1.2 in the gravimetric power and energy density can be achieved when using a conductive carbon composite as the BP material. A modified titanium foil has been proposed by Lang et al.[23] as a possible candidate for BP, though they have investigated the material for a lead-acid battery only. The recent patent by Nagaya et al.[26] proposed the SUS stainless steel as the CC for solid-state cells. However, we show in this model that the gravimetric power density of the bipolar titanium and SUS stainless steel stack lag by a factor of 1.27 and 1.77 respectively compared to the bipolar aluminum stack. Hence, on the basis of gravimetric power and energy density, the carbon composite and aluminum foil are more suitable than titanium and stainless steel as the BP materials.

While metallic conductors such as aluminum and Li have a rather isotropic electronic conductivity, the through-plane electronic conductivity of a carbon composite can be several orders of magnitude lower than the in-plane electronic conductivity. As shown by Fig. 2, the electrical current flows from one unit cell to the next unit cell through the BP. Figure B·2 in the Appendix shows the simulated effects of through-plane electronic conductivity of carbon composite on the gravimetric energy and power densities. Due to a smaller magnitude of applied current densities and a larger stack surface area for the electronic transport in a bipolar stack, the gravimetric energy and power densities are found to be not sensitive to the variation in the through-plane electronic conductivity.

Copper has been used as the negative CC in conventional parallel Li-ion stacks. It is possible to replace the copper foil with Li as the negative CC when Li is used as the NE in a solid-state stack. In this work, we investigate the impact of Li and copper CC on the gravimetric power and energy density of the parallel stack. Here we show that the simulated gravimetric power and energy density of the

parallel Li stack can be 1.77 times higher than parallel copper stack, which can be attributed to the higher mass ratio of active materials in parallel Li stack (53%) compared to parallel copper stack (30%) (see Fig. B·1 in Appendix B).

Stack Temperature Profiles

Whilst the heat generation in a single-layer cell is insignificant because of the small and thermally thin cell, heat generations from a multilayer stack can significantly affect the stack performance. Figure 10 illustrates the model predicted temperature across the surfaces and tabs of the bipolar aluminum and parallel Li stacks under the operating conditions of 3C constant-current discharge from an initial temperature of 298.15 K. In the models, both stacks were cooled by natural air convection across the top surface of the stacks ($h = 5\ \mathrm{W\,m^{-2}\,K^{-1}}$, air temperature = 20 °C) with additional heat dissipation by radiation from the top and bottom of the stacks. The temperature gradients are normalised by the average temperature ($T_{surf} - T_{ave}$) at each time-step for ease in comparing.

As shown by Figs. 10a1 and 10b1, the bipolar and parallel stack show a negligible temperature gradient at the beginning of discharge. While the bipolar aluminum stack shows a negligible temperature gradient throughout discharge, the temperature gradients around the tabs of the parallel Li stack increase. The predicted temperature distribution is consistent with the experimental IR imaging result reported by Kim et al., who recorded the highest temperature gradients near the tabs of a Li-ion polymer battery.[17] The parallel stack shows an average temperature rise of 33.91 K, whereas the average temperature rise of the bipolar stack is 18.51 K. For a large-format parallel Li-ion stack using liquid electrolytes, Yazdanpour et al.[20] showed through experimental measurements that the temperature increase could achieve up to 30 K under a high C-rate discharge. The significant temperature gradients and higher temperature rise of the parallel Li stack are caused by Joule heating due to tabs and CC (see Fig. B·4b in Appendix B).

The parallel stack has a total heat generation of 12.18 kJ whereas the bipolar stack has a total heat generation of only 4.99 kJ. For the given operating condition, the double-coated parallel stack has a higher nominal current compared to the single-sided bipolar stack, leading to a higher heat generation. As shown by Fig. 2, a parallel stack also has external tabs at each unit cell whereas a bipolar stack has only one positive and one negative tab at the two outermost unit cells. Both stack models neglect the contact resistance between the tabs and the external connectors, whose value is dependent on the experimental setup. In reality, the additional contact resistance would aggravate the Joule heating effects.[36]

Advantages and Disadvantages of Bipolar and Parallel Stacks

Although the bipolar stack shows significant advantages over the parallel stack in terms of higher energy densities and lower heat generations, a bipolar stack has a higher risk of stack failure. The failure of one unit cell such as due to delamination or crack propagation does not lead to the failure of an entire parallel stack. On the other hand, failure in one unit cell will certainly cause the failure of the entire bipolar stack. Understanding the failure mechanisms at the microscale will be critical for the successful commercialisation of bipolar solid-state Li-metal batteries for any medium to large scale application.

Secondly, as the total stack current for a bipolar stack is equal to the current of one unit cell, the Couloumbic capacity of the stack does not scale with the number of unit cells inside the stack. In this work, the nominal capacity of 63 cells stacked in series is only 0.12 Ah. Therefore, a thick electrode design with an optimised mass transfer is required to improve the stack capacity. Table III

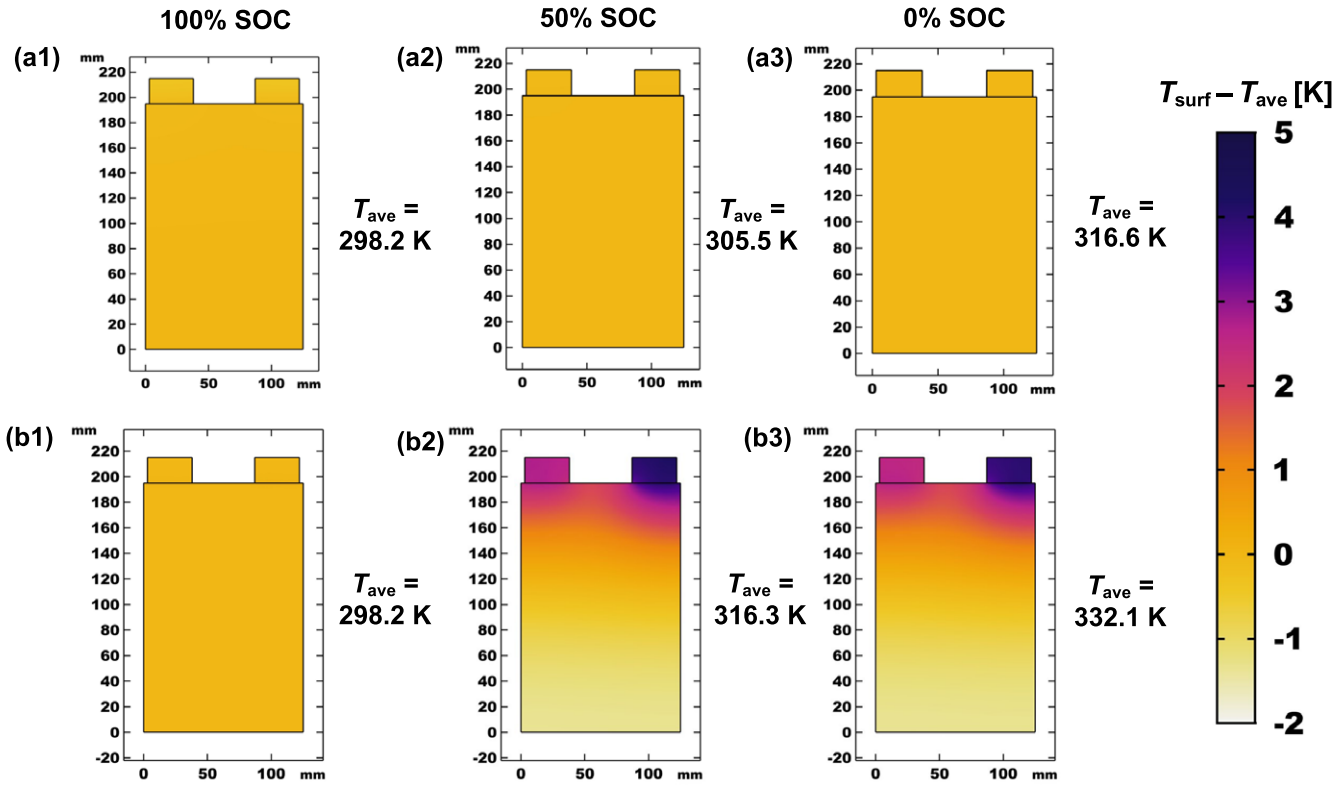


Figure 10. Temperature profile across the surface and tabs of the bipolar and parallel stack at the initial temperature of 298.15 K and 3C constant-current discharge. The temperature distributions are normalised by the average temperature at each time-step to compare the temperature gradients of two different stacks: (a1) Two-dimensional temperature profile of the bipolar stack at 100% SOC, where the average surface temperature is 298.2 K, (a2) at 50% SOC, where the average surface temperature is 305.5 K and (a3) at 0% SOC, where the average surface temperature is 316.6 K. (b1) Surface temperature profile of the parallel stack at 100% SOC (T_{ave} = 298.2 K), (b2) 50% SOC (T_{ave} = 316.3 K) and (b3) 0%SOC (T_{ave} = 332.1 K).

Table III. Advantages and disadvantages of bipolar and parallel stacks.

	Bipolar stack	Parallel stack
Current homogeneity	More uniform current distribution can be achieved across the entire surface area. The bipolar stack uses the entire stack surface area to transfer current from one unit cell to the adjacent unit cell.	Current transferred through the external tabs of the parallel stack causes higher local current densities around the tabs.
Coulombic stack capacity	Limited stack capacity (0.12 Ah) due to the serial connection of each unit cell: A thick PE configuration with an optimised electrode design is necessary to improve the stack capacity.	A high nominal capacity (4 Ah) with a thin PE (6 μm) can be achieved by scaling the number of unit cells (32 double-coated unit cells) in a parallel configuration.
Power and energy density	The volumetric and gravimetric energy densities of the bipolar aluminum stack are higher than those of the parallel Li stack.	The temperature-dependent creep behavior of Li metal implies that Li foils may not be used as the negative CC. If copper foils substitute Li foils as the negative CC, the gravimetric energy and power density decreases by a factor of 1.77.
Heat generations	The heat generation due to Joule heating of the tabs in a bipolar stack is negligible (0.036 W m^{-2}).	Under a 3C constant-current discharge, Joule heating due to tabs in a parallel stack can reach up to 146 W m^{-2}. A higher heat generation in the parallel stack suggests that an effective thermal management is required, which could further reduce the volumetric and gravimetric density of the battery modules at the system level.
Effects of unit cell failure	Reliable bonding of each unit cell is necessary as delamination in one unit cell will cause the failure of the entire bipolar stack.	Failure of one unit cell does not necessarily lead to failure of the entire stack.

summarises the advantages and disadvantages of bipolar and parallel cell stacks.

Conclusions

A two-ways thermally coupled bipolar and parallel solid-state stack model was developed by scaling a single-layer cell model based on dimensionless governing equations and stacking the single-layer cell models in series and in parallel.

The parameter values of the single-layer cell model were obtained from experimental PEIS and GITT measurements at 25 °C, 35 °C, 45 °C and 55 °C. When increasing the operating temperature from 25 °C to 55 °C, the electrolyte resistance decreases by a factor of 10.8, whereas the charge-transfer resistance at the NE and PE interface can be reduced by a factor of 24.4 and 17.5 respectively. A higher operating temperature is shown to have a negligible impact on the diffusion coefficients for high SOCs, but an increase up to a factor of 50 can be observed for low SOCs.

By fixing the thickness of each component in the single unit cell within the same stack volume for both bipolar and parallel stacks, the energy and power densities of both stack configurations can be compared. We used the stack model to study (1) the voltage discharge profiles of bipolar and parallel stacks, (2) the effects of Li volume deformation on stack volumetric power and energy densities, (3) the effects of different CC on gravimetric power and energy densities and (4) the effects of carbon composite through-plane electronic conductivities on the stack gravimetric power and energy densities. The bipolar stack can reach up to 265 V with 63 cells stacked in series, whereas a nominal capacity of 4.23 Ah is achievable with 32 double-coated cells stacked in parallel. A polyurethane spacer was included in the stack design to reduce the internal stress and strain due to the temperature-dependent creep behavior of Li metal. The bipolar aluminum stack has a higher volumetric energy and power density than the parallel Li stack due to the additional required spacer to suppress the volumetric deformation of the Li CC. In a parallel stack, if the copper foils substitute the Li foils as the negative CC in order to reduce volume change, the gravimetric energy and power densities drop by a factor of 1.77. By replacing the BP with different materials in the model, we demonstrate that the bipolar stack with carbon composite and aluminum has higher gravimetric energy and power density than the titanium and stainless steel bipolar stack because of lower densities of carbon composite and aluminum. The impacts of through-plane electronic conductivity of carbon composite BP on the gravimetric energy and power densities of the bipolar stack are found to be negligible due to a smaller magnitude of current densities and a larger stack surface area for the electronic transport in the bipolar stack. In addition to the stack performance metrics determined by this study, cost and manufacturability must also be considered for practical applications in future works.

Through comparing the temperature profiles of the bipolar and parallel stacks under the operating conditions of 3C constant-current discharge from an initial temperature of 25 °C, the parallel stack shows an average temperature rise of 33.91 K, whereas the bipolar stack of only 18.51 K. While Joule heating in a bipolar stack is negligible, in a parallel stack, it can reach 146 W m^{-2}. Therefore, the bipolar stack is more advantageous than the parallel stack in terms of higher energy densities and lower rates of heat generation. However, due to the serial configuration of each unit cell, a delamination or crack propagation in one unit cell will lead to the failure of the entire stack. For this reason, an in-depth understanding of the failure mechanisms will be critical for the successful implementation of the bipolar solid-state Li-metal batteries.

Data Availability

The electrochemical parameters measured in this work are available at https://github.com/mc-git-code/Solid-State-Cell-Parameters, DOI: 10.5281/zenodo.4281060

Acknowledgments

Much appreciated is the funding received from Beijing Institute of Aeronautical Materials (BIAM). The research was performed at the BIAM-Imperial Centre for Materials Characterisation, Processing and Modelling at Imperial College London. The authors would like to thank Dr. Yan Zhao, Dr. Ganesh Madabattula, Dr. Teddy Szemberg O'Connor, Dr. Krishnakumar Gopalakrishnan and Dr. David Howey for helpful discussions. The authors would also like to thank the Reviewer for the constructive feedback in improving the robustness and quality of this work.

Appendix A. Single-layer Cell Model

Dimensional governing equations.—This Section summarises the governing equations of the temperature-dependent single-layer cell model. The details of the derivations can be found in Ref. 13.

Governing equations in the solid electrolyte.—Temperature-dependent current distribution in the SE domain is given by

$$i = -\sigma_{\text{elec}}(\overline{T})\frac{\partial \phi_{\text{elec}}}{\partial z}, \qquad [A\cdot1]$$

where $\sigma_{\text{elec}}(\overline{T})$ is the temperature-dependent electrolyte conductivity and ϕ_{elec} is the electrolyte potential. Current conservation across the SE is defined by

$$\frac{\partial i}{\partial z} = 0. \qquad [A\cdot2]$$

Boundary conditions in the SE domain are

$$\phi_{\text{s}}|_{z=0} = 0, \qquad [A\cdot3]$$

$$\sigma_{\text{elec}}(\overline{T})\frac{\partial \phi_{\text{elec}}}{\partial z}\bigg|_{z=d_{\text{elec}}} = i_{\text{app}}, \qquad [A\cdot4]$$

where ϕ_{s} denotes the reference potential of metallic Li, d_{elec} is the thickness of the SE and i_{app} is the externally applied current density.

Governing equations in the positive electrode.—Molar conservation in the PE domain are

$$\frac{\partial c_{\text{Li}}}{\partial t} = \frac{\partial}{\partial z}\left(D_{\text{Li}}(x_{\text{Li}}, \overline{T})\frac{\partial c_{\text{Li}}}{\partial z}\right), \qquad [A\cdot5]$$

$$D_{\text{Li}}(x_{\text{Li}}, \overline{T})\frac{\partial c_{\text{Li}}}{\partial z}\bigg|_{z=d_{\text{elec}}} = -\frac{i}{F}, \qquad [A\cdot6]$$

$$D_{\text{Li}}(x_{\text{Li}}, \overline{T})\frac{\partial c_{\text{Li}}}{\partial z}\bigg|_{z=d_{\text{elec}}+d_{\text{pos}}} = 0, \qquad [A\cdot7]$$

in which c_{Li} is the Li concentration in the PE, $D_{\text{Li}}(x_{\text{Li}}, \overline{T})$ represents the concentration and temperature-dependent diffusion coefficient in the non-porous PE and d_{pos} denotes the thickness of the PE.

Redox reactions at the electrolyte-electrode interfaces.—Linearised Butler-Volmer expression at the NE-SE interface is

$$i = i_{0,\text{neg}}(\overline{T})\frac{(\alpha_{\text{a}} + \alpha_{\text{c}})F}{R_{\text{gas}}\overline{T}}\eta_{\text{neg}}. \qquad [A\cdot8]$$

The cathodic Tafel's equation at the SE-PE interface is represented by

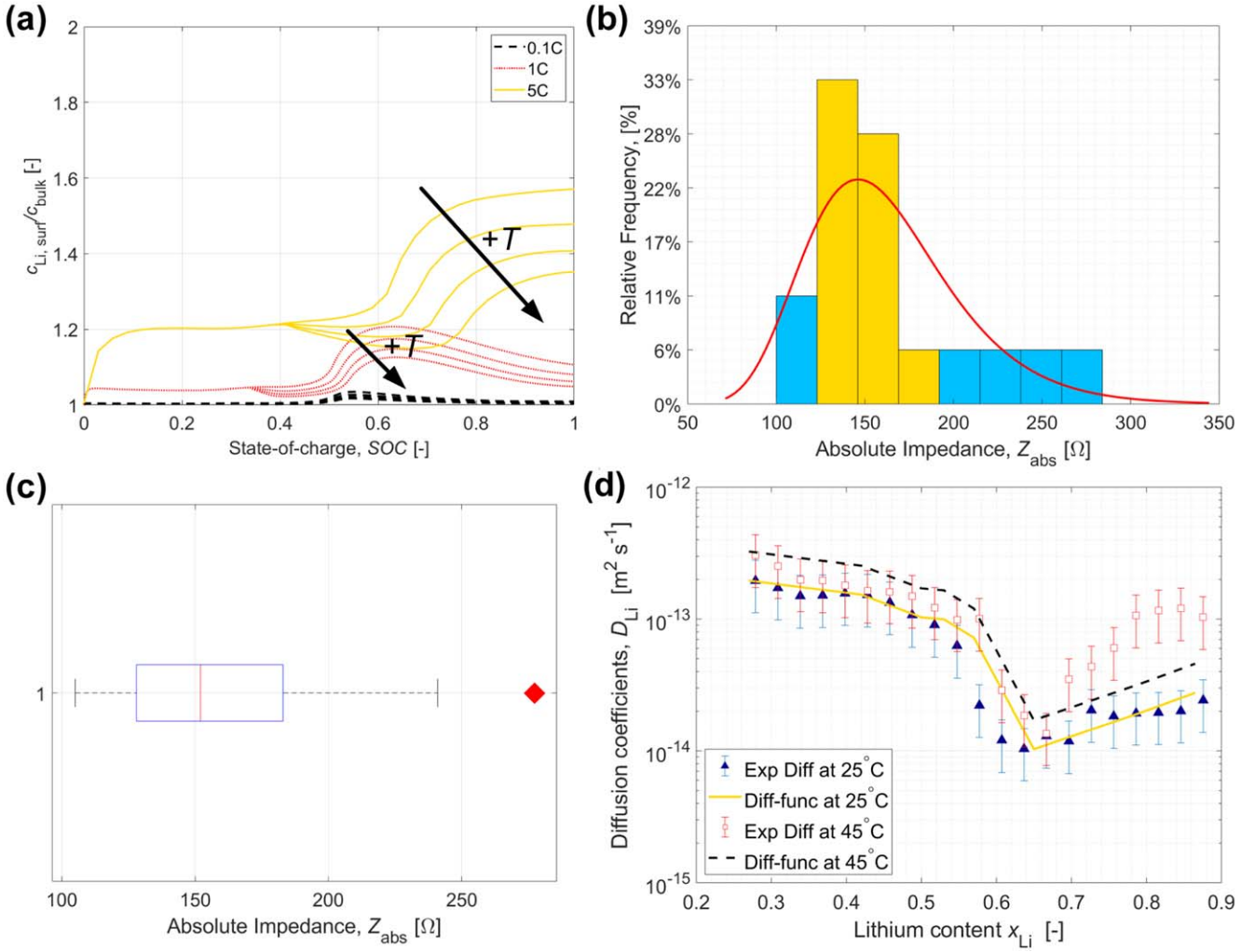


Figure A·1. (a) Comparison of the ratio $c_{Li,surf}/c_{bulk}$ for three C-rates: 0.1C, 1C and 5C. (b) A log-normal statistical analysis to quantify the initial impedance variability of 23 cells: The highlighted yellow bars corresponds to the interquartile range of the boxplot. (c) A representative boxplot of the statistical analysis. (d) Comparison of the approximated function to the experimental measurements at 25 °C and 45 °C.

$$i = -i_{0,\mathrm{pos}}(\overline{T})\left(\frac{c_{\mathrm{Li,surf}}}{c_{\mathrm{bulk}}}\right)\exp\left(\frac{-\alpha_{\mathrm{c}}F\eta_{\mathrm{pos}}}{R_{\mathrm{gas}}\overline{T}}\right). \qquad [\mathrm{A}\cdot9]$$

Alternatively, the cathodic Tafel's equation can be rewritten as follows:

$$i = -i_{0,\mathrm{pos}}(\overline{T})\left(\frac{c_{\mathrm{Li,surf}}}{c_{\mathrm{bulk}}}\right) \times 10^{\frac{\eta_{\mathrm{pos}}}{A_{\mathrm{c}}}}, \qquad [\mathrm{A}\cdot10]$$

where A_c is the cathodic Tafel's slope:

$$A_{\mathrm{c}} = -\frac{2.303R_{\mathrm{gas}}\overline{T}}{\alpha_{\mathrm{c}}F}. \qquad [\mathrm{A}\cdot11]$$

Calculation of overpotentials.—The expressions used to calculate the charge-transfer overpotentials at both interfaces, the ohmic overpotential across the SE and the diffusion overpotential in the PE are given by

$$\eta_{\mathrm{neg/pos}}|_{z\,=\,0,\ z\,=\,d_{\mathrm{elec}}} = \phi_{\mathrm{s}} - \phi_{\mathrm{elec}} - U, \qquad [\mathrm{A}\cdot12]$$

$$\eta_{\mathrm{ohm}} = \phi_{\mathrm{s}}|_{z\,=\,d_{\mathrm{elec}}} - \phi_{\mathrm{s}}|_{z\,=0}, \qquad [\mathrm{A}\cdot13]$$

$$\eta_{\mathrm{diff}} = U_{\mathrm{LCO}}(c_{\mathrm{Li}}) - U_{\mathrm{LCO}}(\overline{c}_{\mathrm{Li}}). \qquad [\mathrm{A}\cdot14]$$

Non-dimensional governing equations.—In this section, dimensionless variables and parameters are introduced, followed by a summary of non-dimensional governing equations. We introduce six dimensionless variables in this work to redefine a dimensionless system of governing equations for the model. The temperature dependence is considered implicitly through the model parameters in these non-dimensional governing equations.

$$\text{length: } z_{\mathrm{n}}'' = \frac{z_{\mathrm{n}}}{L_{\mathrm{z}}}, \qquad [\mathrm{A}\cdot15]$$

$$\text{time: } t'' = \frac{t}{\tau_{\mathrm{d}}}, \qquad [\mathrm{A}\cdot16]$$

$$\text{potential: } \phi_{\mathrm{k}}'' = \frac{F\phi_{\mathrm{k}}}{R_{\mathrm{gas}}\overline{T}}, \quad \mathrm{k} = [\mathrm{elec, s}], \qquad [\mathrm{A}\cdot17]$$

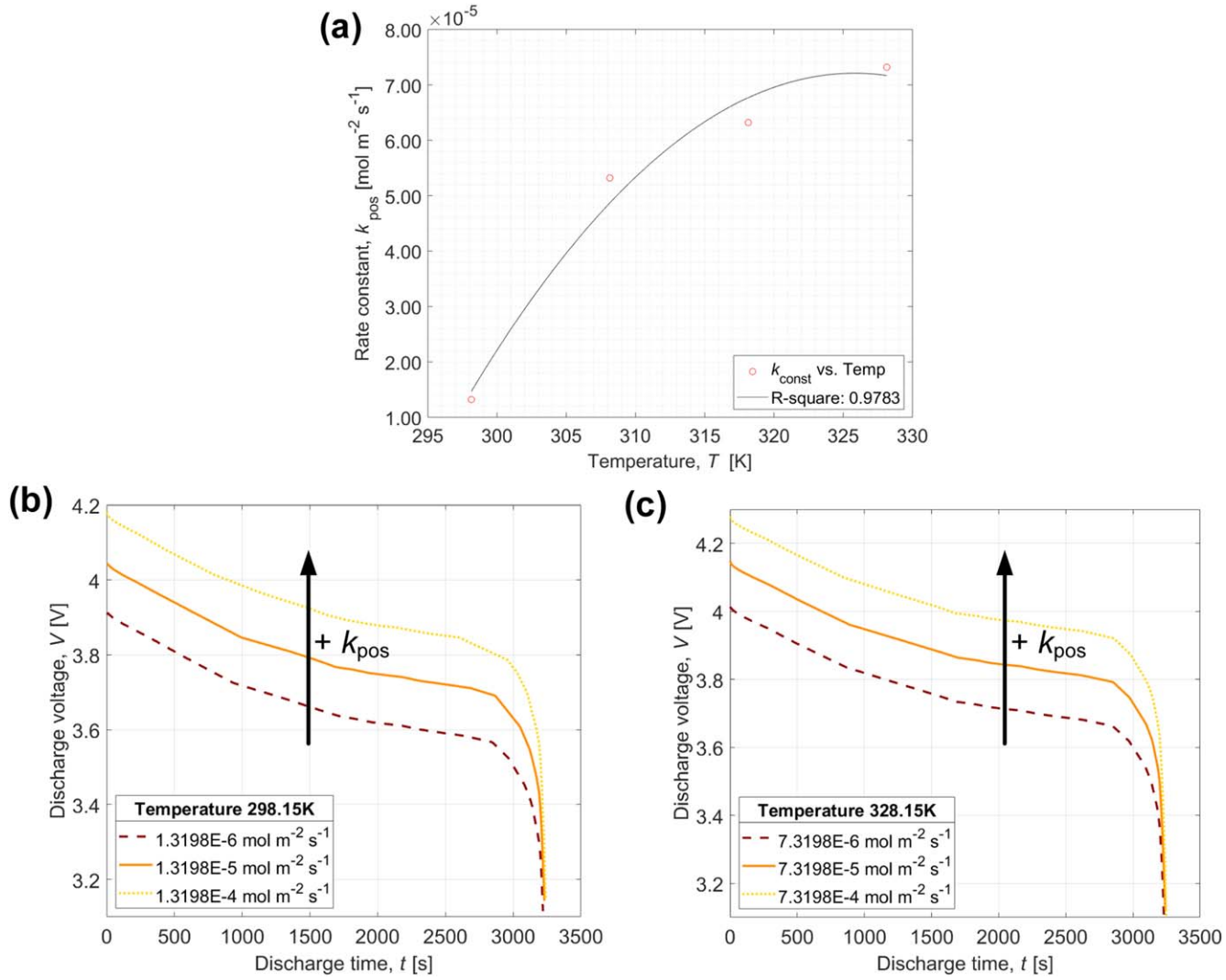


Figure A·2. (a) The fitted rate-constant, k_{pos} as a function of operating temperature. The effect of k_{pos} on the cell discharge voltage curve at 25 °C in Fig. A·2b and at 55 °C in Fig. A·2c. The solid orange lines correspond to the model parameter values chosen in this work.

$$\text{lithium concentration: } c''_{\text{Li}} = \frac{c_{\text{Li}}}{c_{\text{LCO,max}}}, \qquad \text{[A·18]}$$

$$\text{diffusion coefficient: } D''_{\text{Li}} = \frac{\log_{10}(D_{\text{Li}}(x_{\text{Li}}))}{\log_{10}(\max D_{\text{Li}}(x_{\text{Li}}))}, \qquad \text{[A·19]}$$

$$\text{current: } i'' = \frac{i}{i_{\text{cell,ref}}}. \qquad \text{[A·20]}$$

L_z denotes the total thickness of the electrode and the electrolyte, τ_{d} is the discharge timescale and $i_{\text{cell,ref}}$ is the current density of the experimental cell ($i_{\text{cell,ref}} = 0.6154\,\text{mA cm}^{-2}$).

A dimensionless current distribution in the SE domain can be obtained by substituting Eqs. A·15, A·17 and A·20 into Eq. A·1, where σ''_{elec} is the dimensionless electrolyte conductivity:

$$i'' = -\sigma''_{\text{elec}} \frac{\partial \phi''_{\text{elec}}}{\partial z''_{\text{elec}}}. \qquad \text{[A·21]}$$

Similarly, by replacing the dimensional variables in Eq. A·5 with Eqs. A·15, A·16, A·18 and A·19, a dimensionless concentration distribution can be obtained in the PE:

$$\frac{\partial c''_{\text{Li}}}{\partial t''} = \frac{\partial}{\partial z''_{\text{pos}}}\left(D''_{\text{Li}} \frac{\partial c''_{\text{Li}}}{\partial z''_{\text{pos}}}\right). \qquad \text{[A·22]}$$

$$\left.\frac{\partial c''_{\text{Li}}}{\partial z''}\right|_{z''=z''_{\text{elec}}} = -\frac{i''}{D''_{\text{Li}}}, \qquad \text{[A·23]}$$

$$\left.\frac{\partial c''_{\text{Li}}}{\partial z''}\right|_{z''=z''_{\text{elec}}+z''_{\text{pos}}} = 0. \qquad \text{[A·24]}$$

Assuming $\alpha_{\text{neg}} = \alpha_{\text{pos}} = 0.5$, the dimensionless linearised Butler-Volmer and cathodic's Tafel's expressions can be obtained by substituting Eqs. A·17 and A·20 into Eqs. A·8 and A·9 as

$$i'' = \frac{i_{0,\text{neg}}}{i_{\text{cell,ref}}} \eta''_{\text{neg}}, \qquad \text{[A·25]}$$

$$i'' = -\frac{i_{0,\text{pos}}}{i_{\text{cell,ref}}}\left(\frac{c_{\text{Li,surf}}}{c_{\text{bulk}}}\right) \exp\left(-\frac{\eta''_{\text{pos}}}{2}\right). \qquad \text{[A·26]}$$

Model parameterisation.—Figure A·1a illustrates the comparison of the ratio $c_{Li,surf}/c_{bulk}$ for three C-rates. For low C-rate such as 0.1C, this term remains approximately 1. With increasing C-rates, the surface diffusion limitations become significant.

Figure A·1b shows the log-normal statistical analysis to quantify the variability of 23 cells by the initial PEIS measurements after three cycles at 1 mA of constant-current charge and discharge. These variations were also observed in the experimental results by Fabre et al. and Larfaillou et al.,[39,44] in which three semi-circles in the EIS measurements were observed by Fabre et al.[44] and four semi-circles were proposed by Larfaillou et al.[39] on different cells of the same chemistry. All of the PEIS measurements were first normalised by excluding the influence from the contact resistance (e.g. all of the semi-circles begin from the [0,0] point). Figure A·1c illustrates the corresponding boxplot of the statistical analysis. From the boxplot, the first quartile, median and third quartile can be determined, which are 128 Ω, 152 Ω and 183 Ω respectively. Based on the dataset from 23 measurements, the variability corresponding to the first and third quartile is 42.97%. Therefore, initial cell screening is necessary to minimize this variability. Because of the relatively large variability, the PEIS, GITT, $\partial U(x_{Li})/\partial T$ and constant-current discharge experiments in this work were performed on a single cell.

Figure A·1d shows a comparison of the approximated temperature- and concentration-dependent diffusion function (Eq. 36) to the experimental measurements at 25 °C and 45 °C. A maximum deviation of 9.023×10^{-14} m^2 s^{-1} can be observed between the approximated function and the measurements, which is due to the trade-off to capture the temperature-dependent diffusion coefficient at high and low SOCs. This deviation causes a difference up to 5% between the simulated and measured cell voltage toward low SOCs, as shown in Fig. 7a.

Figure A·2a shows the fitted rate-constant as a function of temperature. The rate constant increases with increasing temperatures, but the rate of increase decreases with temperature. Figures A·2b and A·2c illustrate the effect of this parameter on the cell discharge voltage at 25 °C and 55 °C. The simulated cell voltages were found to be sensitive to this parameter. The cell voltage changes significantly when k_{pos} is modified by one order of magnitude.

Appendix B. Stack Model

Mass and volume balance of the stacks.—Table B·I summarises the electrical and thermal properties of different CC and BP. Figure B·1 shows the mass and volume ratios of the parallel and bipolar stacks. Substituting the metallic Li foil by copper foils as the negative CC reduce the spacer contribution from 53% to 43% (Figs. B·1d and B·1e) but increases the the mass ratio of CC from 33% to 62% (Figs. B·1a and B·1b). For the bipolar aluminum stack, the spacers and seals account for 44% of the volume of the stack but only 5% of its mass (Figs. B·1c and B·1f). Figure B·2 shows the predicted gravimetric energy and power densities of the bipolar stack using different values of through-plane electronic conductivities. Despite a lower through-plane electronic conductivity of carbon composite compared to in-plane electronic conductivity, these effects were found to be negligible on the stack performance due to a larger stack surface area and a lower magnitude of current densities in a bipolar stack.

Table B·II shows the calculation of the mass and volume balance for the parallel stack with Li negative CC and the bipolar stack with aluminum BP. In this calculation, each intermediate parallel double-coated unit cell shares the same negative CC, whereas each intermediate bipolar unit cell shares the BP. Polyurethane spacers are included in both stacks to account for the possible volume deformation due to metallic Li. In addition to the spacer, a fluoroelastomer seal is included in the bipolar stack to prevent direct contact between adjacent BP and therefore an internal short-circuit.

Effective ohmic resistance of the parallel stack current collectors.—Figure B·3 illustrates the side view of the current flow in the CC of a parallel stack. As the current moves in perpendicular and in-

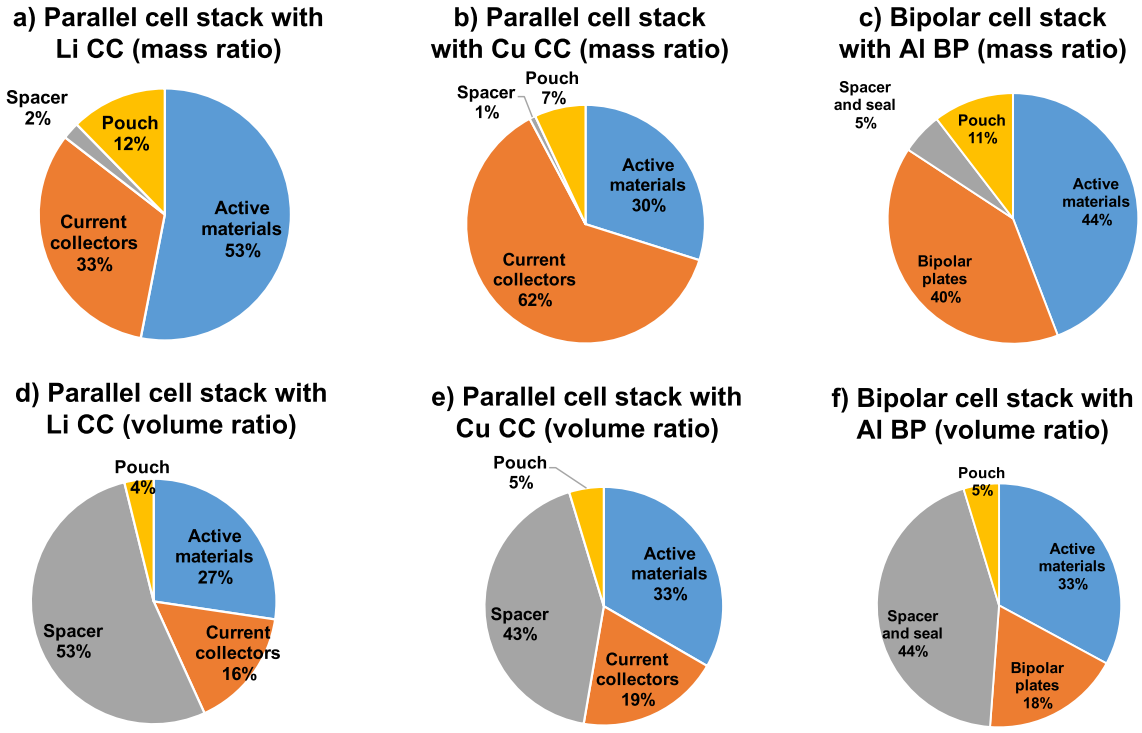


Figure B·1. Mass and volume ratio of the parallel and bipolar stacks: (a) Mass ratio of the parallel lithium stack. (b) Mass ratio of the parallel stack with copper foil as the negative CC. (c) Mass ratio of the bipolar stack with aluminum foil as the BP material. (d) Contribution to the total volume of the stack by its various components: (d) Lithium CC and (e) copper CC in the parallel stack, (f) aluminum BP in the bipolar stack.

Table B·I. Electrical and thermal properties of different current collectors and bipolar plates.

Materials	Electronic conductivity (S m^{-1})	Density (kg m^{-3})	Specific heat capacity (J kg^{-1} K^{-1})	Thermal conductivity (W m^{-1} K^{-1})	References
Parallel stack					
Lithium foil	1.1×10^7	534	3582	81.8	32, 41
Copper foil	5.96×10^7	8960	385	398	20, 32
Bipolar stack					
Carbon fibres	$1000 - 10^5$	1820	598	6	18, 27, 29
Aluminium foil	3.78×10^7	2700	897	238	20, 32
Titanium foil	1.79×10^6	4540	523	18.85	57–60
Stainless steel	1.37×10^6	7930	502	14.64	61

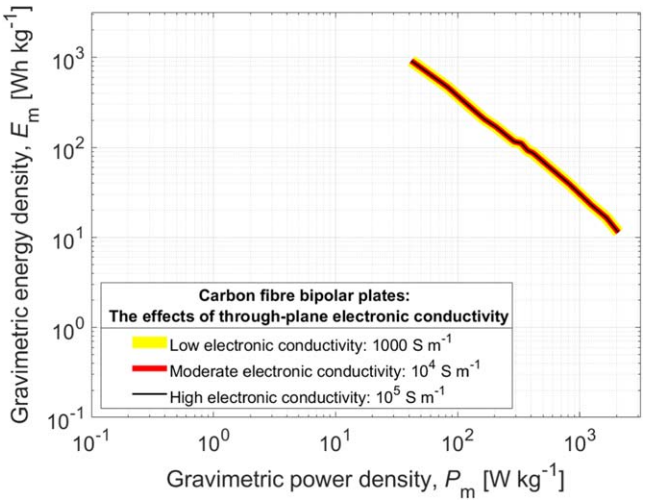


Figure B·2. The effects of different through-plane electronic conductivities of the carbon composite BP on the gravimetric energy and power densities of the bipolar stack.

plane along the CC, a two-dimensional electrical model obeying Ohm's law is used to calculate the effective resistance due to electronic conductivity in the CC. The calculated effective resistances from the 2D model are given in Table B·III and compared to the analytical 1D in-plane resistance, $R_{CC,Par}$ calculated by

$$R_{CC,Par} = \frac{L_y}{\sigma_{CC} A_{cross,CC}}, \quad [B·1]$$

where L_y is the height of the pouch, σ_{CC} is the electronic conductivity of the CC and $A_{cross,CC}$ is the cross-sectional area of the the CC ($A_{cross,CC} = d_{CC} L_x$).

Estimated heat generations of the stacks.—Figure B·4a shows the estimated heat generation of the bipolar and parallel stack at the initial temperature of 25 °C and 40 °C. The total amount of heat over the entire SOC for both stacks can be calculated from areas under the heat versus time curve. The bipolar aluminum stack has an estimated total heat generation of 4.99 kJ. On the other hand, the parallel Li stack has a higher total heat generation of 12.18 kJ. This difference can be explained by the higher nominal current of the double-coated parallel stack compared to the single-sided bipolar stack and the

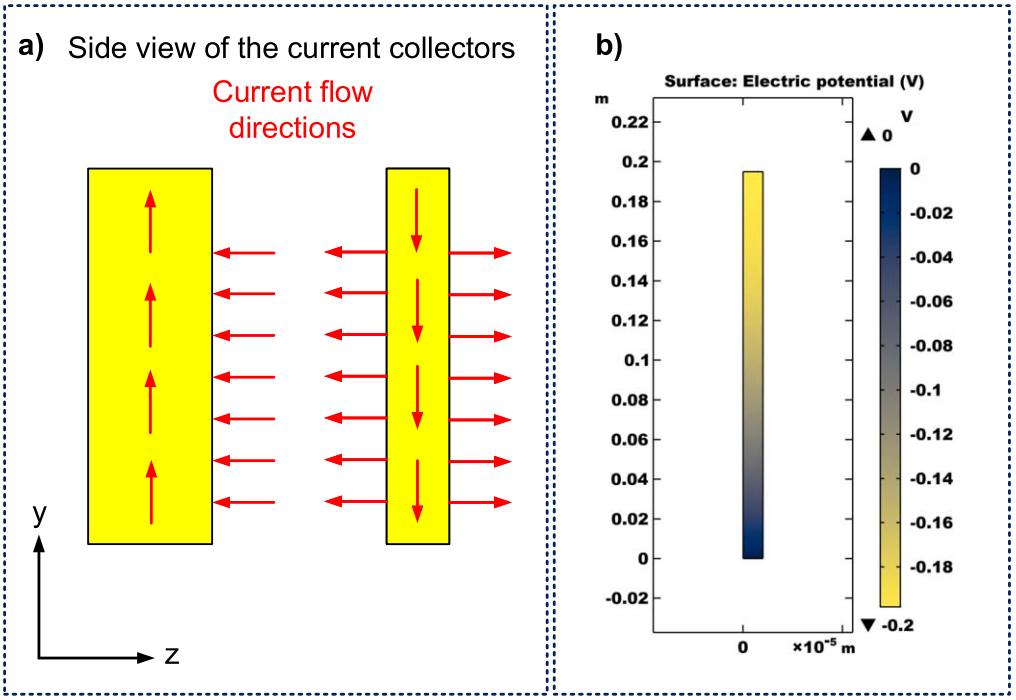


Figure B·3. (a) Side view of the current flow in the CC of a parallel stack. The thickness of each CC in the middle is halved to account for the double-coated configuration. The electrical current first flows perpendicular to the surface area of the CC and then in-plane along the CC to the external tab. (b) A two-dimensional electrical model, where the effective resistance due to the electronic transport is calculated from the applied current density and the computed average voltage drop in the CC.

Table B·II. Mass and volume balance of the bipolar aluminum and parallel lithium stacks.

Parallel stack				
Component	Thickness	Volume	Density	Mass
Lithium current collector	10 μm	0.2438 cm^3	0.534 g cm^{-3}	0.130 g
Lithium negative electrode	10 μm	0.2438 cm^3	0.534 g cm^{-3}	0.130 g
LiPON solid electrolyte	2 μm	0.0488 cm^3	2.680 g cm^{-3}	0.131 g
$LiCoO_2$positive electrode	6 μm	0.1463 cm^3	3.121 g cm^{-3}	0.456 g
Aluminium current collector	10 μm	0.2438 cm^3	2.700 g cm^{-3}	0.658 g
Double-coated unit cell	56 μm	1.3650 cm^3		2.223 g
Copper tab	10 μm	0.0070 cm^3	8.960 g cm^{-3}	0.063 g
Aluminium tab	10 μm	0.0070 cm^3	2.700 g cm^{-3}	0.019 g
Double-coated unit cell with tabs	56 μm[a)]	1.3790 cm^3		2.304 g
Polyurethane spacer	2.231 mm	54.3806 cm^3	0.035 g cm^{-3}	1.903 g

Table B·II. (Continued).

Component	Thickness	Volume	Density	Mass
Parallel stack				
Aluminate pouch	0.162 mm	3.9488 cm^3	2.700 g cm^{-3}	10.662 g
Parallel stack (32 units)	4.195 mm	102.7081 cm^3		86.499 g
Bipolar stack				
Lithium negative electrode	10 μm	0.2438 cm^3	0.534 g cm^{-3}	0.130 g
LiPON solid electrolyte	2 μm	0.0488 cm^3	2.680 g cm^{-3}	0.131 g
$LiCoO_2$positive electrode	6 μm	0.1463 cm^3	3.121 g cm^{-3}	0.457 g
Aluminium bipolar plate	10 μm	0.2438 cm^3	2.700 g cm^{-3}	0.658 g
Single unit cell	28 μm	0.6827 cm^3		1.376 g
Copper tab	10 μm	0.007 cm^3	8.960 g cm^{-3}	0.063 g
Aluminium tab	10 μm	0.007 cm^3	2.700 g cm^{-3}	0.019 g
First unit cell with copper tab	28 μm[a)]	0.6897 cm^3		0.911 g
Last unit cell with aluminum tab	28 μm[a)]	0.6897 cm^3		1.395 g
Fluoroelastomer seal	3.332 mm[b)]	2.3324 cm^3	1.825 g cm^{-3}	4.257 g
Polyurethane spacer	1.426 mm	34.7588 cm^3	0.035 g cm^{-3}	1.217 g
Aluminate pouch	0.162 mm	3.9488 cm^3	2.700 g cm^{-3}	10.662 g
Bipolar stack (61 units + first unit + last unit)	3.352 mm	84.0641 cm^3		102.3780 g

a) The overall thickness of the stack does not include the thickness of the tabs. b) The seal spans between the tabs and does not contribute the overall stack thickness.

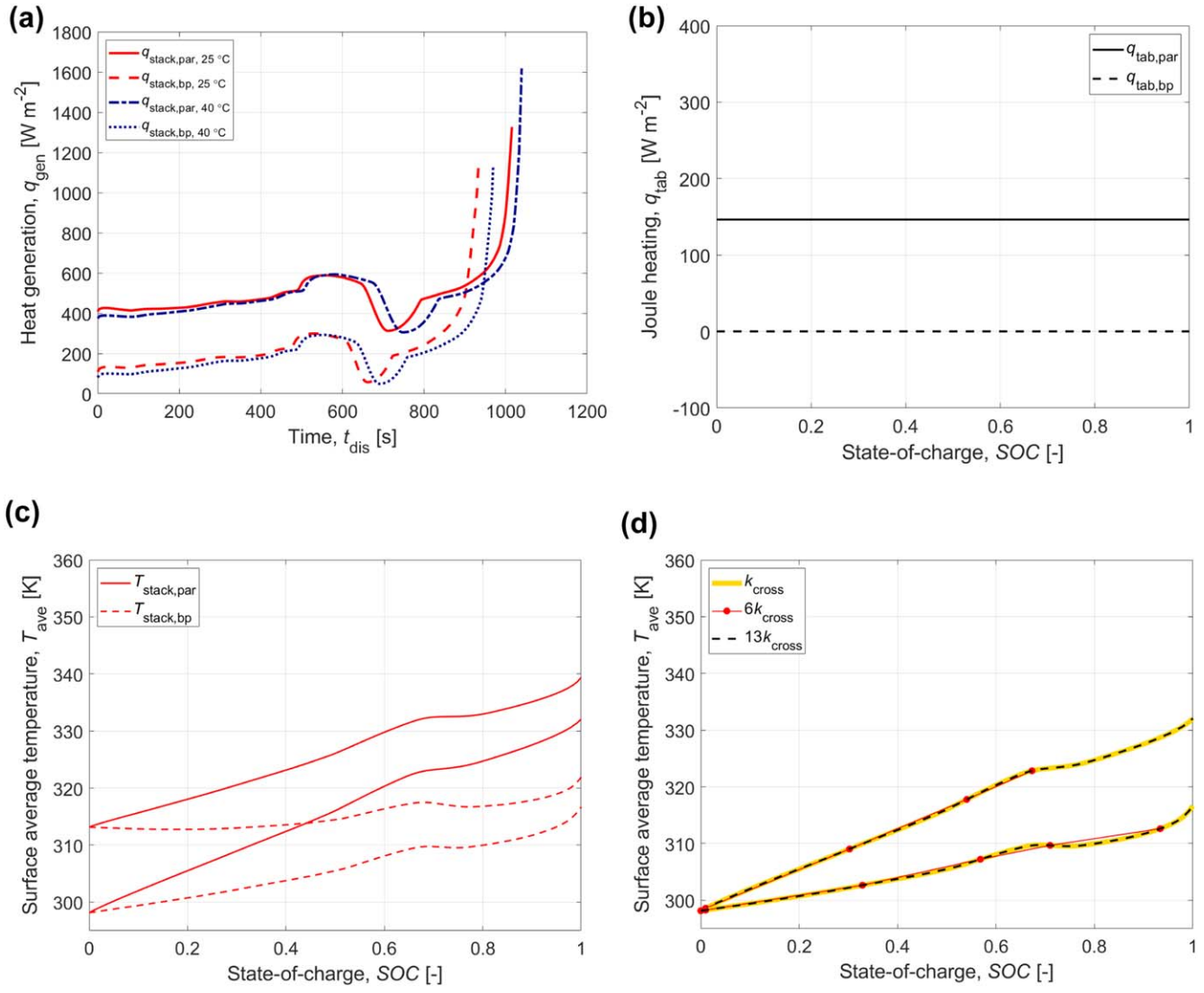


Figure B·4. (a) The estimated heat generation in the bipolar aluminum stack and the parallel lithium stack under 3C constant-current discharge from an initial temperature of 298.15 K and 313.15 K. (b) The Joule heating effects in the parallel (solid black lines) and bipolar stacks (dashed black lines). (c) The temperature change profile of the parallel (solid red lines) and bipolar stacks (dashed red lines). (d) The effects of different solid electrolyte thermal conductivity on the surface average temperature change.

Table B·III. Comparison of 2D effective resistances to 1D in-plane resistances.

Materials	2D effective resistance (Ω)	1D in-plane resistance (Ω)
	Copper current collector	
Two-sided current flow	3.49×10^{-3}	2.62×10^{-3}
One-sided current flow	8.72×10^{-4}	
	Li current collector	
Two-sided current flow	1.89×10^{-2}	1.42×10^{-2}
One-sided current flow	4.73×10^{-3}	
	Aluminium current collector	
Two-sided current flow	5.50×10^{-3}	4.13×10^{-3}

effects of Joule heating. Figure B·4b compares the heat generations due to Joule heating of the tabs for both stacks. The heat generation at tabs is significant for the parallel stack (146.4 W m^{-2}) and almost negligible for the bipolar stack (0.036 W m^{-2}). This difference can be explained by the tab configurations as illustrated by Fig. 2. With a larger discharge current of 28.8 A for the parallel stack compared to the discharge current of 0.75 A for the bipolar stack, the Joule heating effects become dominant for the parallel stack. Figure B·4c shows the average temperature change from an initial temperature of 298.15 K and 313.15 K. For a constant-current discharge from an initial temperature of 298.15 K, the surface temperature of the parallel stack increases to 332.1 K whereas the surface temperature of the bipolar stack increases to 316.3 K. Figure B·4d shows that the effect of thermal conductivities of the SE on the average surface temperature is negligible for both bipolar and parallel stacks.

List of Symbols

Greek Symbols

α	Charge transfer coefficient	—
ϵ	Surface emissivity	—
η''	Dimensionless overpotential	—
η_{neg}	Overpotential at the NE and SE interface	V
η_{pos}	Overpotential at the PE and SE interface	V
ϕ_k''	Dimensionless potential	—
ϕ_{elec}	Electrolyte potential	V
ϕ_{neg}	Negative electrode potential	V
ϕ_{pos}	Positive electrode potential	V
ρ	Material density	kg m^{-3}
σ''_{elec}	Dimensionless electrolyte conductivity	—
σ_{BP}	Bipolar plate electronic conductivity	S m^{-1}
$\sigma_{elec,ref}$	Reference electrolyte conductivity	S m^{-1}
σ_{neg}	Li electronic conductivity	S m^{-1}
σ_{pos}	LCOelectronic conductivity	S m^{-1}
σ_{tab}	Tab electronic conductivity	S m^{-1}
σ_{elec}	Electrolyte conductivity	S m^{-1}

Latin Symbols

ΔS	Entropy	J mol^{-1} K^{-1}
$\frac{\partial U(x_{Li})}{\partial T}$	Entropic heat coefficient	mV K^{-1}
A_{BP}	Bipolar plate surface area	m^2
A_c	Cathodic Tafel's slope	mV
$A_{tab,cross}$	Tab cross-sectional area	m^2
C_p	specific heat capacity at constant pressure	J kg^{-1} K^{-1}
D_{Li}	Diffusion coefficient of Li^+	m^2 s^{-1}
E_A	Activation energy	J mol^{-1}
$L_{tab,y}$	Tab height	m
L_z	Total domain thickness	m
N_{BP}	Number of unit cells in a bipolar stack	—
N_{Par}	Number of unit cells in a parallel stack	—
Q_{conv}	Heat dissipation by convection	W
$Q_{gen,tot}$	Total heat generation	W
Q_{irrev}	Irreversible heat generation	W

(Continued).

List of Symbols

Q_{rad}	Radiative heat dissipation	W
Q_{rev}	Reversible heat generation	W
R_{AM}	Active materials ohmic resistance	Ω
R_{BP}	Bipolar plate ohmic resistance	Ω
R_{CC}	Current collector ohmic resistance	Ω
R_{tab}	Tab ohmic resistance	Ω
T_{amb}	Ambient temperature	K
T_{ref}	Reference temperature (T_{ref} = 298.15 K)	K
V_{BP}	Bipolar stack voltage	V
V_{cell}	Cell volume	m^3
c''_{Li}	Positive electrode dimensionless Li concentration	—
c_{Li}	Electrode Li concentration	mol m^{-3}
$c_{LCO,max}$	LCO maximum lithium concentration	mol m^{-3}
d_{BP}	Bipolar plate thickness	m
$d_{cell,BP}$	Bipolar cell thickness	m
$d_{cell,Par}$	Parallel cell thickness	m
d_{neg}	Thickness of the negative electrode	m
d_{pouch}	Pouch thickness	m
d_{elec}	Thickness of the solid electrolyte	m
d_{pos}	Thickness of the positive electrode	m
h	heat transfer coefficient	W m^{-1} K^{-1}
i''	Dimensionless current	—
i''_0	Dimensionless exchange current density	—
i_0	Exchange current density	A m^{-2}
i_{app}	Externally applied current density	A m^{-2}
i_{cell}	Cell current density	A m^{-2}
i_{stack}	Stack current density	A m^{-2}
k_{BP}	Bipolar plate thermal conductivity	W m^{-1} K^{-1}
k_{CC}	Current collector thermal conductivity	W m^{-1} K^{-1}
k_{elec}	LiPON thermal conductivity	W m^{-1} K^{-1}
k_{LCO}	LCO thermal conductivity	W m^{-1} K^{-1}
k_{pouch}	Pouch thermal conductivity	W m^{-1} K^{-1}
k_{eff}	Effective thermal conductivity	W m^{-1} K^{-1}
k_{pos}	Electrochemical rate constant	mol m^{-2} s^{-1}
t''	Dimensionless time	—
z''_n	Dimensionless length	—

Superscripts

$''$	Dimensionless variable/parameter

Subscripts

AM	Active Material
app	Applied
a	Anode
BP	Bipolar
cell	Single-layer cell
conv	Convection
c	Cathode
diff	Diffusion
eff	Effective
gen	Generation

(Continued).

List of Symbols

irrev	Irreversible
max	Maximum
neg	Negative
ohm	Ohmic
pos	Positive
ref	Reference
rev	Reversible
stack	Cell stack
s	Solid
tot	Total

ORCID

Mei-Chin Pang https://orcid.org/0000-0002-6138-3530
Huizhi Wang https://orcid.org/0000-0003-2287-0544
Monica Marinescu https://orcid.org/0000-0003-1641-3371
Gregory J. Offer https://orcid.org/0000-0003-1324-8366

References

1. J. B. Bates, N. J. Dudney, G. R. Gruzalski, R. A. Zuhr, A. Choudhury, C. F. Luck, and J. D. Robertson, *Journal of Power Sources*, **43**, 103 (1993).
2. M. Ogawa, R. Kanda, K. Yoshida, T. Uemura, and K. Harada, *Journal of Power Sources*, **205**, 487 (2012).
3. Y. Kato, S. Hori, T. Saito, K. Suzuki, M. Hirayama, A. Mitsui, M. Yonemura, H. Iba, and R. Kanno, *Nat. Energy*, **1**, 652 (2016).
4. R. Koerver, I. Aygün, T. Leichtweiß, C. Dietrich, W. Zhang, J. O. Binder, P. Hartmann, W. G. Zeier, and J. Janek, *Chemistry of Materials*, **29**, 5574 (2017).
5. G. Li and C. W. Monroe, *Phys. Chem. Chem. Phys.*, **21**, 20354 (2019).
6. D. P. Finegan et al., *Nat. Commun.*, **6**, 6924 (2015).
7. J. Schnell, T. Günther, T. Knoche, C. Vieider, L. Köhler, A. Just, M. Keller, S. Passerini, and G. Reinhart, *Journal of Power Sources*, **382**, 160 (2018).
8. R. Pfenninger, M. Struzik, I. Garbayo, E. Stilp, and J. L. M. Rupp, *Nat. Energy*, **4**, 475 (2019).
9. K. Kariatsumari, Toyota announces 4-layer all-solid-state battery (2010), www.tech.nikkeibp.co.jp/dm/english/NEWS_EN/20101122/187553/.
10. Y. Gambe, Y. Sun, and I. Honma, *Sci. Rep.*, **5**, 359 (2015).
11. S. Ito, S. Fujiki, T. Yamada, Y. Aihara, Y. Park, T. Y. Kim, S.-W. Baek, J.-M. Lee, S. Doo, and N. Machida, *Journal of Power Sources*, **248**, 943 (2014).
12. R. Bock, M. Onsrud, H. Karoliussen, B. G. Pollet, F. Seland, and O. S. Burheim, *Energies*, **13**, 253 (2020).
13. M.-C. Pang, Y. Hao, M. Marinescu, H. Wang, M. Chen, and G. J. Offer, *Physical chemistry chemical physics: PCCP*, **21**, 22740 (2019).
14. J. S. Newman and K. E. Thomas-Alyea, *Electrochemical Systems* (Wiley, Hoboken, N.J. and Chichester) 3rd ed. (2004).
15. E. J. F. Dickinson and G. Hinds, *J. Electrochem. Soc.*, **166**, F221 (2019).
16. EiG ePLB-C020 Datasheet, Energy Innovation Group (EiG) Ltd., South Korea.
17. U. S. Kim, C. B. Shin, and C.-S. Kim, *Journal of Power Sources*, **189**, 841 (2009).
18. R. M. Lafollette, *Bipolar battery cells, batteries and methods*, US Patent 5,582,937 (1996).
19. T. Liu, Y. Zhang, C. Chen, Z. Lin, S. Zhang, and J. Lu, *Nat. Commun.*, **10**, 1965 (2019).
20. M. Yazdanpour, P. Taheri, A. Mansouri, and M. Bahrami, *J. Electrochem. Soc.*, **161**, A1953 (2014).
21. M. Wolter, M. Fritsch, S. Börner, B. Capraro, and K. Nikolowski, "EMBATT bipolar lithium battery concept—Approach to increase energy density for automotive application." *Fraunhofer-Institut für Keramische Technologien und Systeme IKTS* (2019).
22. R. M. LaFollette and D. N. Bennion, *J. Electrochem. Soc.*, **137**, 3693 (1990).
23. X. Lang, D. Wang, and J. Zhu, *Journal of Power Sources*, **272**, 176 (2014).
24. R. A. Marsh, P. G. Russell, and T. B. Reddy, *Journal of Power Sources*, **65**, 133 (1997).
25. V. Livshits, A. Blum, E. Strauss, G. Ardel, D. Golodnitsky, and E. Peled, *Journal of Power Sources*, **97–98**, 782 (2001).
26. K. Nagaya, M. Kamiya, and S. Okayama, *Method for testing all solid state battery, method for producing all solid state battery, and method for producing battery pack*, US2019/0331736A1 (2019).
27. T. Tian, *PhD Thesis*, Mechanical (and Materials) Engineering—Dissertations, Theses, and Student Research. 27., University of Nebraska-Lincoln (2011).
28. T. W. Ebbesen, H. J. Lezec, H. Hiura, J. W. Bennett, H. F. Ghaemi, and T. Thio, *Nature*, **382**, 54 (1996).
29. T. W. Ebbesen, *Annu. Rev. Mater. Sci.*, **24**, 235 (1994).
30. S. C. Chen, C. C. Wan, and Y. Y. Wang, *Journal of Power Sources*, **140**, 111 (2005).
31. T. M. Bandhauer, S. Garimella, and T. F. Fuller, *Journal of Power Sources*, **158**, R1-R25 (2011).
32. L. Song and J. W. Evans, *J. Electrochem. Soc.*, **147**, 2086 (2000).
33. F. Xu, C. Frétigny, D. Fournier, L. Belliard, S. Vincent, B. Perrin, S. Martin, C. Secouard, and J.-Y. Duquesne, *J. Appl. Phys.*, **113**, 244304 (2013).
34. H. Maleki, S. Al Hallaj, J. R. Selman, R. B. Dinwiddie, and H. Wang, *J. Electrochem. Soc.*, **146**, 947 (1999).
35. W. Mei, H. Chen, J. Sun, and Q. Wang, *Sustainable Energy Fuels*, **3**, 148 (2019).
36. Y. Zhao, L. B. Diaz, Y. Patel, T. Zhang, and G. J. Offer, *J. Electrochem. Soc.*, **166**, A2849 (2019).
37. A. Hales, L. B. Diaz, M. W. Marzook, Y. Zhao, Y. Patel, and G. Offer, *J. Electrochem. Soc.*, **166**, A2383 (2019).
38. M. Shadman Rad, D. L. Danilov, M. Baghalha, M. Kazemeini, and P. H. L. Notten, *Electrochimica Acta*, **102**, 183 (2013).
39. S. Larfaillou, D. Guy-Bouyssou, F. Le Cras, and S. Franger, *Journal of Power Sources*, **319**, 139 (2016).
40. M. Ménétrier, I. Saadoune, S. Levasseur, and C. Delmas, *Journal of Materials Chemistry*, **9**, 1135 (1999).
41. T. Gray, N. Mann, and M. Whitby, (Oct 31, 2019), Electrical Conductivity of the elements https://periodictable.com/Properties/A/ElectricalConductivity.an.html.
42. H. Yang, J.-Y. Yang, C. N. Savory, J. M. Skelton, B. J. Morgan, D. O. Scanlon, and A. Walsh, *The journal of physical chemistry letters*, **10**, 5552 (2019).
43. T. H. Wan, M. Saccoccio, C. Chen, and F. Ciucci, *Electrochimica Acta*, **184**, 483 (2015).
44. S. D. Fabre, D. Guy-Bouyssou, P. Bouillon, F. Le Cras, and C. Delacourt, *J. Electrochem. Soc.*, **159**, A104 (2012).
45. K. Smith and C.-Y. Wang, *Journal of Power Sources*, **160**, 662 (2006).
46. K. E. Thomas, C. Bogatu, and J. Newman, *Solid State Ionics*, **148**, A570 (2001).
47. X.-F. Zhang, Y. Zhao, Y. Patel, T. Zhang, W.-M. Liu, M. Chen, G. J. Offer, and Y. Yan, *Physical chemistry chemical physics: PCCP*, **19**, 9833 (2017).
48. W. S. LePage, Y. Chen, E. Kazyak, K.-H. Chen, A. J. Sanchez, A. Poli, E. M. Arruda, M. D. Thouless, and N. P. Dasgupta, *J. Electrochem. Soc.*, **166**, A89 (2019).
49. A. Masias, N. Felten, R. Garcia-Mendez, J. Wolfenstine, and J. Sakamoto, *J. Mater. Sci.*, **54**, 2585 (2019).
50. J. Kasemchainan, S. Zekoll, D. Spencer Jolly, Z. Ning, G. O. Hartley, J. Marrow, and P. G. Bruce, *Nat. Mater.*, **18**, 1105 (2019).
51. J.-M. Doux, H. Nguyen, D. H. S. Tan, A. Banerjee, X. Wang, E. A. Wu, C. Jo, H. Yang, and Y. S. Meng, *Adv. Energy Mater.*, **10**, 1903253 (2020).
52. C. Zhang, Y. Liu, X. Jiao, S. Xiong, and J. Song, *J. Electrochem. Soc.*, **166**, A3675 (2019).
53. R. Li, D. Ren, D. Guo, C. Xu, X. Fan, Z. Hou, L. Lu, X. Feng, X. Han, and M. Ouyang, *J. Electrochem. Soc.*, **166**, A4106 (2019).
54. G. Nagasubramanian, R. Jungst, and D. Doughty, *Journal of Power Sources*, **83**, 193 (1999).
55. Y. V. Mikhaylik and J. R. Akridge, *J. Electrochem. Soc.*, **150**, A306 (2003).
56. A. Du Pasquier, I. Plitz, S. Menocal, and G. Amatucci, *Journal of Power Sources*, **115**, 171 (2003).
57. R. W. Powell and R. P. Tye, *Journal of the Less-common metals*, **3**, 226 (1961).
58. A. Yoshida, Y. Omae, T. Kurita, and S. Washio, *International Journal of Thermophysics*, **21**, 513 (2000).
59. A. Augustyn et al., Titanium: Chemical Element https://www.britannica.com/science/titanium.
60. I. Golobic, J. Petkovsek, and D. Kenning, *International Journal of Heat and Mass Transfer*, **55**, 1385 (2012).
61. World Material, SUS304 Stainless steel material properties, chemical composition, meaning https://www.theworldmaterial.com/sus304-stainless-steel-material/.